Notice

Manuscript details

Title: 2-D P-SV and SH spectral element modelling of seismic wave propagation in non-linear media with pore-pressure effects

Authors: Elif ORAL (IRSN and IFSTTAR), Céline Gélis (IRSN), and Luis Fabian Bonilla (IFSTTAR)
Contact: elifo @caltech.edu

2D P-SV and SH spectral element modelling of seismic wave propagation in nonlinear media with pore-pressure effects

Elif Oral[1,2], Céline Gélis[1] and Luis Fabián Bonilla[2]

[1]Institut de Radioprotection et de Sûreté Nucléaire, Fontenay-aux-Roses, France
[2]Institut Français des Sciences et Technologies des Transports, de l'Aménagement et des Réseaux, Marne-la-Vallée, France

Abstract

It has long been recognised that the effects of superficial geological layers, or site effects, can play a major role on the seismic ground motion at the free surface. In this study, we compute wave propagation in a 2D asymmetrical basin considering both soil nonlinearity and pore-pressure effects. Equations of elastodynamics of wave propagation are solved using the spectral element method (SEM). The geometry of the basin gives rise to basin-edge generated waves, that are different for in-plane (P-SV) and out-of-plane (SH) wave propagation and resulting in different nonlinear response. Moreover, the excess-pore pressure development in superficial liquefiable layers (effective stress analysis) brings larger deformation and loss of strength than the analysis without pore-pressure effects (total stress analysis). The coupling of vertically propagating waves and the waves specifically generated in 2D model leads to waves whose amplitude and duration are higher than the 1D case. This multi-dimensional effect increases material nonlinearity. Such complex wavefield provokes larger deformation and higher pore-pressure rise that cannot be predicted by 1D modelling. Therefore, our paper suggests the use of multi-dimensional modelling while studying seismic wave propagation in both linear and nonlinear complex media.

Keywords: Earthquake ground motions; Numerical modelling; Site effects; Wave propagation; Elasticity and anelasticity

1 Introduction

It is widely known that site effects play a major role on the amplification, duration and spatial variability of the earthquake ground motion. The destructive impact of site effects has been experienced by considerable human and material losses in past events such as the 1985 Michoacan, Mexico (Campillo et al., 1989), the 1995 Hyogoken-Nambu, Japan (Tokimatsu et al., 1996), the

1999 İzmit, Turkey (Bakir et al., 2002) and the 2015 Gorkha, Nepal (Chiaro et al., 2015) earthquakes. The nature and geometry of sedimentary structures may lead to strong diffraction of waves on curved boundaries and formation of basin-edge generated waves (Sanchez-Sesma et al. 1985; Kawase and Aki, 1989; Chávez-García et al., 1994). Such an effect could further prolong the wave propagation and intensify the damage where waves pass through (Bard and Bouchon, 1985). Therefore, the effect of multi-dimensional site geometry should be considered in site-specific studies.

In spite of the many observations worldwide, in order to understand the physical processes behind seismic wave propagation in complex media, numerical modelling is often needed. There are numerous studies of wave propagation that assume that the material behaves linearly (e.g. Olsen and Archuleta, 1996; Delavaud, 2007; Smerzini et al., 2011; Peyrusse et al., 2014). Yet, large ground motion could trigger material nonlinearity, and if the sediments are water-saturated, pore-pressure effects may further modify the ground motion (i.e. Aguirre and Irikura, 1997; Iai et al., 1995; Bonilla et al., 2005; Bonilla et al., 2011; Laurendeau et al., 2017). Significant spatial variability of ground motion can arise from excess-pore pressure development in presence of liquefiable soils as observed in the 2011 earthquake of Christchurch, New Zealand where widespread liquefaction was reported at different sites in the near field (Bradley and Cubrinovski, 2011).

Conversely, relatively few studies focus on wave propagation in nonlinear media. The 2D analyses of Takemiya and Adam (1998) highlight the nonlinearity effect on coastal zones during the 1995 Kobe earthquake by attenuation of ground acceleration for frequencies over 1 Hz. Roten et al. (2012) model the 3D wave propagation in Wasatch Fault (USA) including 1D soil nonlinearity. They conclude that the calculated ground motion at near-source region gets closer to the prediction models only when high-frequency ground-motion damping due to soil nonlinearity is accounted for. Other studies (Bonilla et al., 2006; Stupazzini et al., 2009; Gandomzadeh, 2011; Martino et al., 2015) compare linear and nonlinear approaches, revealing the significant attenuation of multi-dimensional basin response under high nonlinearity. In some of these studies, the energy content of the modelled ground motion is shown to shift to lower frequencies than the natural frequency, and hence medium velocity is reduced and ground motion may last longer. Such nonlinearity effects in multi-dimensional media have been shown to be strongly dependent on the complexity and the amplitude of the source (Gélis and Bonilla, 2012; 2014). For example, Dupros et al. (2010) report that the increase of earthquake magnitude results in enhanced nonlinearity and more permanent displacement in 3D analyses of the French Riviera model.

Even though the importance of the effects of soil nonlinearity and pore-pressure development on ground motion is generally acknowledged, to which extent these effects could control the surface motion in complex media has not yet been explicitly studied. A better understanding of this aspect is necessary to improve the interpretation of earthquake ground-motion recordings and hence to increase the quality of seismic hazard analyses. The objective of this paper is to study the effects of nonlinearity on 2D P-SV and SH wave propagation, with particular attention devoted to pore-pressure effects. For this purpose, we employ the 2D spectral element code SEM2DPACK (version 2.3.8; Ampuero, 2002), which is available as open source code (detailed in Data and Resources section). This code has previously been used to model the dynamic rupture of non-planar faults and seismic wave radiation (Madariaga et al., 2006),

fault reflections from fluid-infiltrated faults (Haney et al., 2007), nonlinear wave propagation in damaged rocks (Lyakhovsky et al., 2009), wave propagation around a prototype nuclear waste storage tunnel (Smith and Snieder, 2010), benchmarks for wave propagation in heterogeneous media (O'Brien and Bean, 2011) and dynamic rupture modelling of the 2012 Sumatra earthquake (Meng and Ampuero, 2012). Within the scope of this study, we have implemented new features into SEM2DPACK to address the nonlinear behaviour of surficial soil layers.

In Oral et al. (2017), we conducted 1D (one-dimensional) - 3C (three-component) spectral element modelling of seismic wave propagation in nonlinear media and performed validation tests of our approach through comparison with earthquake recordings on a liquefaction test site in California (Wildlife Refuge Liquefaction Array; WRLA). This work follows-up on Oral et al. (2017), extending the modelling to 2D. Soil nonlinearity is approximated by the Masing-Prager-Ishlinski-Iwan (MPII) rheology (Iwan, 1967). MPII approach models material nonlinearity by a set of nested yield surfaces consisting of linear elastic springs and Coulomb friction elements. As an input, it only requires the shear modulus reduction ratio as a function of shear strain, which is readily obtained from laboratory data or from the literature for a wide range of soil classes (Vucetic and Dobry, 1991; EPRI, 1993; Ishibashi and Zhang, 1993; Darendeli, 2001). Furthermore, we use the liquefaction front model of Iai et al. (1990) to take into account excess-pore pressure development in liquefiable soils. By doing so, we are able to model the sudden changes of dilatant/contractive behaviour of cohesionless soils due to cyclic mobility under undrained conditions. The liquefaction front model is based on an empirical relation that correlates pore-pressure changes to the shear work produced during wave propagation. It requires only few parameters that can be obtained from laboratory data or numerical analyses (Iai et al., 1990; Iai et al., 1995; Bonilla et al., 2005; Roten et al., 2013; 2014). For viscoelastic attenuation in the medium, the Liu and Archuleta (2006) model is employed, which considers the total energy dissipation in visco-elastoplastic soil models calculated as the sum of viscoelastic attenuation and hysteretic attenuation (due to the strength weakening as a function of strain in the nonlinear model) similarly to Assimaki et al. (2011), Gélis and Bonilla (2012; 2014) and Oral et al. (2017). The set of parameters required as model input comprises general physical soil properties (such as shear strength and liquefaction resistance). Therefore, the applicability of our numerical model is not merely limited to individual sites with precise data; the findings presented in this work are also helpful to understand and to reduce uncertainties in site-specific ground-motion assessments for other areas.

This paper is organised as follows: firstly, we briefly present the spectral element method and the constitutive material models. As a preliminary study, the viscoelastic basin response is computed for in-plane (P-SV) and out-of-plane (SH) wave propagation. Secondly, the nonlinear response of a 2D sedimentary basin model is analysed and compared to the viscoelastic case, and the effect of pore-pressure development on basin response is investigated through the comparison of different cases (nonlinearity with/without pore-pressure effects). Differences between nonlinear effects triggered in P-SV and SH models are pointed out. In the last section, differences in the nonlinear basin response for the assumptions of 1D and 2D geometries are discussed. Lastly, we offer perspectives and directives for future studies.

2 Numerical Scheme and Constitutive Models

The spectral element approximation is based on the decomposition of the domain into non-overlapping elements Ω_e (segments in 1D, quadrangles in 2D and hexahedra in 3D). In each element Ω_e, Gauss-Lebatto-Legendre (GLL) integration points are defined. Lagrange polynomials are then chosen to define an orthogonal basis, which enables the SEM to have a spectral convergence, making it a very precise numerical method (Faccioli et al., 1997; Komatitsch and Vilotte, 1998; Festa and Vilotte, 2005; Delavaud, 2007). In our case, the system of equation of wave propagation is expressed by velocity-stress formulation. The time discretisation follows the leap-frog scheme. To ensure the stability of this time-marching solver, the time step has to satisfy the Courant-Friedrichs-Lewy (CFL) condition. Here the controlling value definition is adopted from Delavaud (2007), in which the computed CFL number is based on minimum spacing between GLL nodes of spectral element. To avoid artificial wave dispersion, the minimum element size d_{min} is constrained by the relation $d_{min} \leq \lambda_{min} N/ppw$ where λ_{min} is the shortest wavelength propagating in the medium, N is the polynomial degree and ppw is the number of grid points per wavelength (Seriani and Priolo, 1991; 1993). We use 0.3 as the controlling value of CFL and set 5 GLL points (corresponding to a 4^{th} polynomial degree) for ppw = 5 for all the applications in this paper.

The propagation of pressure (P) and shear (S) waves in a 2D vertical plane can be defined in two ways in SEM2DPACK by considering (1) only in-plane P waves and the vertical component of S waves (SV), or (2) only the out-of-plane, horizontal component of S waves (SH). For the remainder of this paper, P-SV and SH models denote the first and second case, respectively. For P-SV waves, the elastodynamic equation of wave motion is written in a vertical plane (x,z) in terms of horizontal and vertical partial terms of external force (f_x and f_z for horizontal and vertical directions, respectively), stress tensor σ (σ_{xx}, σ_{zz}, σ_{xz}) and time derivatives of velocity (v_x and v_z for horizontal and vertical directions, respectively) as follows:

$$\rho \frac{\partial v_x}{\partial t} = (\frac{\partial \sigma_{xx}}{\partial x} + \frac{\partial \sigma_{xz}}{\partial z}) + f_x \tag{1}$$

$$\rho \frac{\partial v_z}{\partial t} = (\frac{\partial \sigma_{zz}}{\partial z} + \frac{\partial \sigma_{xz}}{\partial x}) + f_z \tag{2}$$

For SH waves, the elastodynamic equation of wave motion is expressed as:

$$\rho \frac{\partial v_y}{\partial t} = (\frac{\partial \sigma_{xy}}{\partial x} + \frac{\partial \sigma_{yz}}{\partial z}) + f_y \tag{3}$$

where v_y is the out-of-plane (x,z) velocity field, and f_y is the force acting in the same direction as v_y.

We implement different soil constitutive models into the 2D SEM scheme. MPII nonlinear constitutive model of Iwan (1967) is used following the implementation of Joyner (1975). In Oral et al. (2017), the implemented MPII model holds for 3D soil nonlinearity and only non-zero components are used for 1D wave propagation. We use the same formulation for the 3D soil nonlinearity model. Non-zero components are determined with respect to the P-SV or SH

wave propagation model. The shear modulus degradation is approximated by the hyperbolic model proposed by Hardin and Drnevich (1972). Equation (4) shows the relation between shear modulus G and shear strain γ for this model, where G_0 is the elastic shear modulus and γ_{ref} is the reference shear strain defined as the ratio between the shear strength and the elastic shear modulus:

$$\frac{G}{G_0} = \frac{1}{1 + \gamma/\gamma_{ref}} \tag{4}$$

The liquefaction front model of Iai et al. (1990) is implemented for modelling pore-pressure effects. A detailed explanation about the coupling of MPII model and the liquefaction front model is given in Pham (2013) and Oral (2016). At each time step of the simulation, shear modulus and reference strain are calculated based on the current pore-pressure rise. Then, an updated characteristic backbone curve is constructed accounting for the current values of parameters of MPII model. Verification of the implementation of the viscoelastic and nonlinear constitutive models based on comparison of 1D and 2D models is detailed in Supplementary Appendix A (supplementary material is available to download with the online version of the paper).

3 Nonlinear response of a 2D sedimentary basin model

3.1 Basin properties

We use the same 2D basin model as in Gélis and Bonilla (2014). The model domain has a length of 2000 m and a depth of 250 m, Figure 1. The sedimentary basin has a depth of 225 meters and it is surrounded by bedrock. The basin width varies from 563 m at the surface to 110 m at the base. The left boundary is represented by a straight slope that gives rise to sharp changes along this basin edge, most notably close to the surface. The basin has an elliptic shape at its right boundary. Such an asymmetrical shape was proposed by Lacave and Lemeille (2006) to describe the general shape of Alpine valleys.

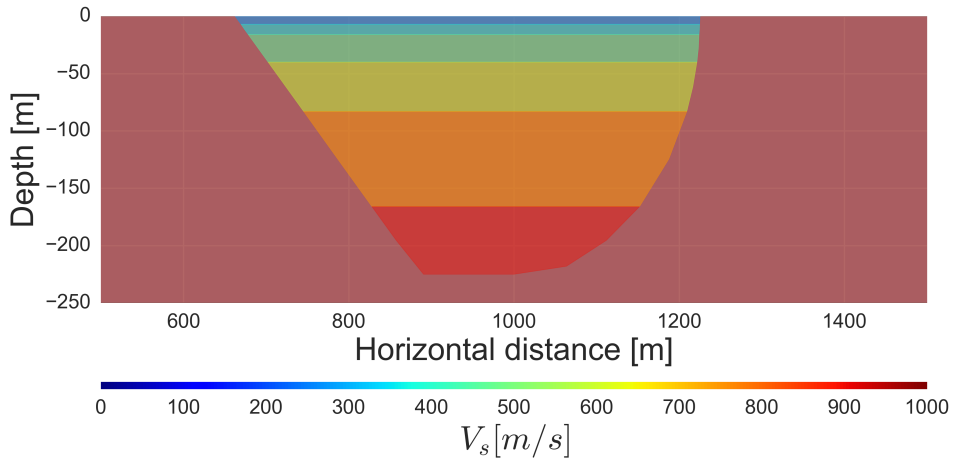

Figure 1: Shear wave velocity profile of the 2D sedimentary basin model. The bedrock shear wave velocity is 2000 m/s.

The model further consists of six soft layers inside the sedimentary basin. Shear velocity increases gradually towards the bottom of the basin. In Gélis and Bonilla (2014), two different velocity models are compared to assess the influence of the velocity distribution on the basin response. In the first model, velocity gradually changes within a soil layer, so that each point at a given depth is defined by a different velocity. In the second model, the basin is divided into layers of constant velocity, which are derived from the velocities of the first model. In their study, the basin response at the surface is shown to be weakly sensitive to constant versus gradually increasing velocities in each layer, as compared to the effect of the soil constitutive model. For convenience, we assume homogeneous soil layers in terms of shear velocity profile in our 2D model.

To determine whether the seismic behaviour of our basin model is close to 1D or 2D in terms of resonance pattern, simple considerations of the basin properties (basin geometry and velocity contrast between the sedimentary layers and the bedrock) can give first indications. In Bard and Bouchon (1985), the nature of specific resonance patterns in 2D sedimentary deposits is investigated for a homogeneous and sinusoidal-shaped basin. 2D resonance produces considerably larger amplifications and longer duration of propagation compared to 1D. The authors have shown that the existence of resonance modes (for P, SV and SH waves) in 2D models is strongly dependent on the shape ratio (ratio of basin depth and width) and velocity contrast with respect to the bedrock. In shallow earth structures, laterally propagating surface waves dominate the ground motion and locally 1D resonances may occur at bedrock/sediment interfaces. In deeper structures, 2D resonance pattern is expected due to the interference of surface waves and vertically propagating waves. In Bard and Bouchon (1985), a curve constrained by the basin properties separates the 1D resonance and lateral propagation of surface waves from the 2D-resonance regime for SH wave propagation. By calculating the shape ratio (0.79) and minimum and maximum velocity contrasts (2.2 and 7.1, respectively) of our basin model, the resultant point remains inside the 2D-resonance regime for both lower and upper limits of the velocity contrasts. Such a result indicates that SH wave propagation in our 2D model should be dominated by the 2D resonance mode of the basin.

Gélis and Bonilla (2012) demonstrated the strong dependence of the basin response on the soil constitutive model by comparing viscoelastic and visco-elastoplastic models exhibiting various degrees of amplitude and complexity of input motion. In their study, the nonlinear soil model was taken to be independent of pressure, and nonlinear curves from EPRI (1993) with different level of nonlinearity were adopted for each layer in the basin. In our study, we consider pressure-dependent soil properties so that nonlinearity changes with depth within a given layer (owing to the effect of confining stress). Nonlinearity parameters of GLL points on a spectral element depend on the depth of the point. Thus, the initial shear modulus of each GLL point is multiplied by a coefficient of $(\frac{\sigma'}{\sigma'_{mid}})^{0.5}$ where σ' is the initial effective stress at the point and σ'_{mid} is the effective confining stress at mid-layer. The water table is set to GL-2 m and is located inside the first layer. Although water table depth is likely to differ horizontally in reality, in this paper, we consider a water table level that is spatially uniform.

The values of shear and pressure wave velocities (V_s and V_p), mass density ρ, quality factors for pressure and shear wave propagation Q_p and Q_s, reference frequency and thickness are taken from Gélis and Bonilla (2014), Table 1.

Table 1: Soil properties of the 2D basin model (after Gélis and Bonilla, 2014).

Layer	$V_s[m/s]$	$V_p[m/s]$	$\rho[kg/m^3]$	Q_s	Q_p
1	278.5	923.7	1800	20	40
2	362.4	1202.0	1800	20	40
3	456.9	1515.4	1800	20	40
4	585.2	1940.9	1800	20	40
5	749.8	2486.8	1800	20	40
6	897.5	2976.7	1800	20	40
Bedrock	2000.0	4163.3	2200	100	200

We suppose that the first two layers are capable of generating pore-pressure excess. We also suppose that the medium composition is identical, with the distinction made only through the P and S wave velocities. Such a configuration implies that the two layers exhibit identical plastic features (i.e. friction and phase transformation angle, and dilatancy parameters; see Table 2). Failure line angle ϕ_f is greater for deeper soils as confining pressures at mid-layer σ'_{mid} increases with depth. Also, the coefficient of Earth at rest is set to 1, such that the initial consolidation is isotropic.

Table 2: Consolidation properties and dilatancy parameters for the 2D model.

Layer	Depth range [m]	$\phi_f[deg]$	$\sigma'_{mid}[kPa]$	$\phi_p[deg]$	w_1	p_1	p_2	S_1
1	0-7	35	47.040	24	5.0	0.6	1.2	0.01
2	7-16	35	109.760	24	5.0	0.6	1.2	0.01
3	16-40	38	239.120	-	-	-	-	-
4	40-83	38	501.760	-	-	-	-	-
5	83-166	40	995.680	-	-	-	-	-
6	166-225	40	1552.320	-	-	-	-	-

The liquefaction susceptibility is represented by the liquefaction resistance curve. This curve is determined by a series of stress-controlled experimental/numerical experiments. In these

tests, soil is loaded under different cyclic stress ratios (CSR, defined as the ratio of applied deviatoric stress to effective mean stress). The liquefaction limit is defined as the number of loading cycles triggering 5 % peak-to-peak of shear strain (corresponding to an axial strain of 2.5 %). The liquefaction resistance curve for a layer is constructed by assembling the number of loading cycles which are calculated for different applied cyclic stress ratios in the numerical tests. One example of such numerical stress-controlled tests is detailed in Appendix B1.

Following Iai et al. (1995), we build a liquefaction curve for the liquefiable layers of our model. Nonlinearity parameters are obtained from a trial-and-error procedure constraining these liquefaction curve, and are listed in Table 2. The number of loading cycles triggering 5 % of shear strain under four different levels of loading (cyclic stress ratio) are plotted in Figure 2. The initial effective mean stress is calculated as 47.040 kPa and 109.760 kPa at the mid-layer depths of layer 1 and 2, respectively. As seen in this figure, 12 loading cycles are required to initiate liquefaction in layer 1 for a stress ratio of 0.17, whereas approximately 4 cycles are necessary for a stress ratio of 0.24. Comparing the two curves, layer 1 liquefies after being subjected to fewer loading cycles than layer 2 for a given CSR.

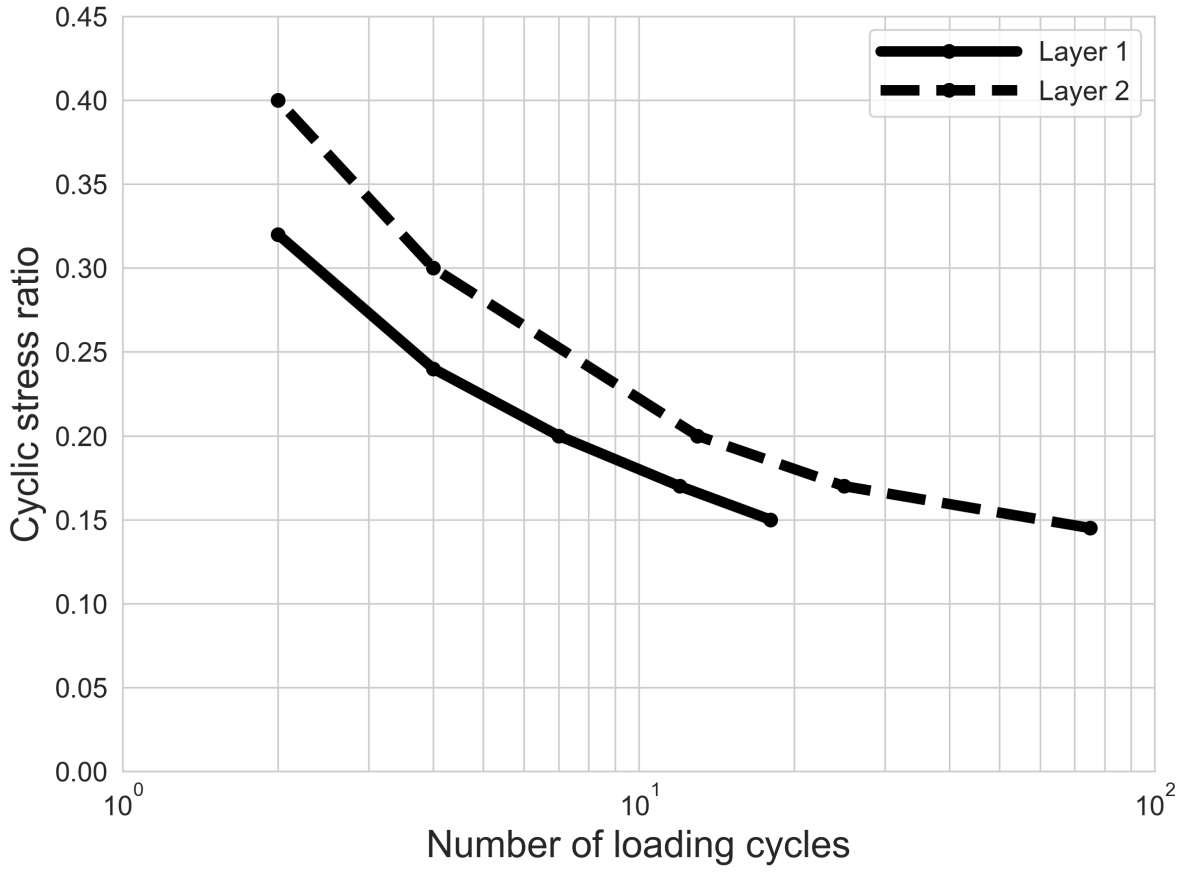

Figure 2: Liquefaction resistance curves for layer 1 (dashed line) and layer 2 (solid line) of the 2D model.

3.2 Numerical model

Since the soil nonlinearity is taken into account in the analyses of this paper, the medium has to be spatially oversampled compared to the linear case. Following Gélis and Bonilla (2012; 2014) and Oral et al. (2017), we first assume that the minimum shear velocity does not decrease to a value less than one-fourth of the initial shear velocity, and then verify that this assumption is valid at the end of the simulation.

For the lateral boundaries of the simulation domain, periodic boundary conditions were adopted. The upper boundary is set to a free surface. An absorbing boundary condition (following the P1 approximation of Stacey, 1988) is adopted for the bottom boundary at GL-250 m. The incident wave field is inserted at this depth, and all vertically down-going waves are absorbed (Delavaud et al., 2006). Through additional tests performed on linear and nonlinear cases, we verified that no undesired reflections (with the potential to significantly change the results) are generated as a result of the prescribed absorbing boundary condition, and that no energy is supplemented to the medium through the periodic boundaries.

As an input motion, a truncated Gaussian synthetic signal is taken as input motion. This signal was provided by the E2VP benchmark of the EUROSEISTEST project material (Mauffroy et al., 2015), which has the benefit of being short in time (impulsive) while exhibiting a broadband frequency content. The acceleration-time history and the corresponding Fourier amplitude are shown in Figure 3. The PGA of the incident wave field corresponds to 0.1 g (before filtering is applied; it approximately equals 0.075 g after filtering), and hence, 0.2 g at the free surface. The signal is filtered on the frequency band of 0.2-10 Hz by a Butterworth filter. The duration of all of the simulations is set to 7 s with a time step of 2×10^{-5} s.

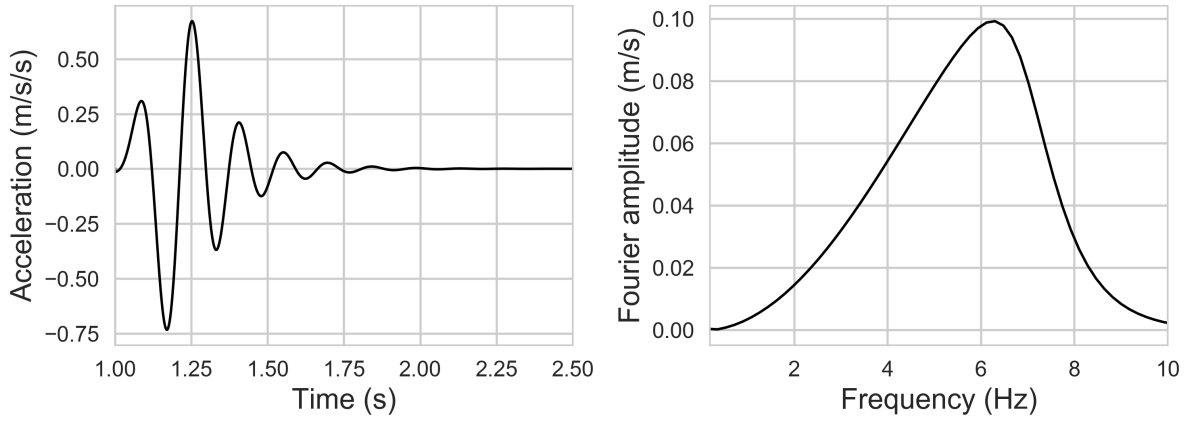

Figure 3: Acceleration-time histories (left) and Fourier amplitude (right) of the input signal.

3.3 Results

3.3.1 Viscoelastic response of the 2D basin model

Viscoelasticity is defined to be pressure dependent in our model, so that the soil properties in a spectral element depend on the confining pressure applied at its depth. The solution of

the viscoelastic case is taken as a reference case in the discussion of the basin response in the presence of nonlinear soil. The verification of the viscoelasticity model for the 2D basin model is provided in Appendix A together with the verifications of the implementation of other constitutive models in SEM2DPACK. First, we analyse the velocity-time histories recorded at the free surface. Figure 4 displays the velocity wavefield of the horizontal components at the free surface of the P-SV model (top) and the SH model (bottom). The seismic stations are situated between 500 and 1500 m from the left boundary with a spacing of 10 m. The influence of the basin asymmetry on both models is apparent from the greater angle of wave reflection at the left side of the basin after the arrival of the first waves (after 1.5 s). Then, strong reflection of waves travelling across the basin width continues during roughly 4 seconds in both models. Wave propagation generated at the basin margins after 3 s is more pronounced in the SH model than in the P-SV model. Attenuation of basin waves occurs within 2 seconds for the two models, while this duration is 0.5 seconds in the bedrock.

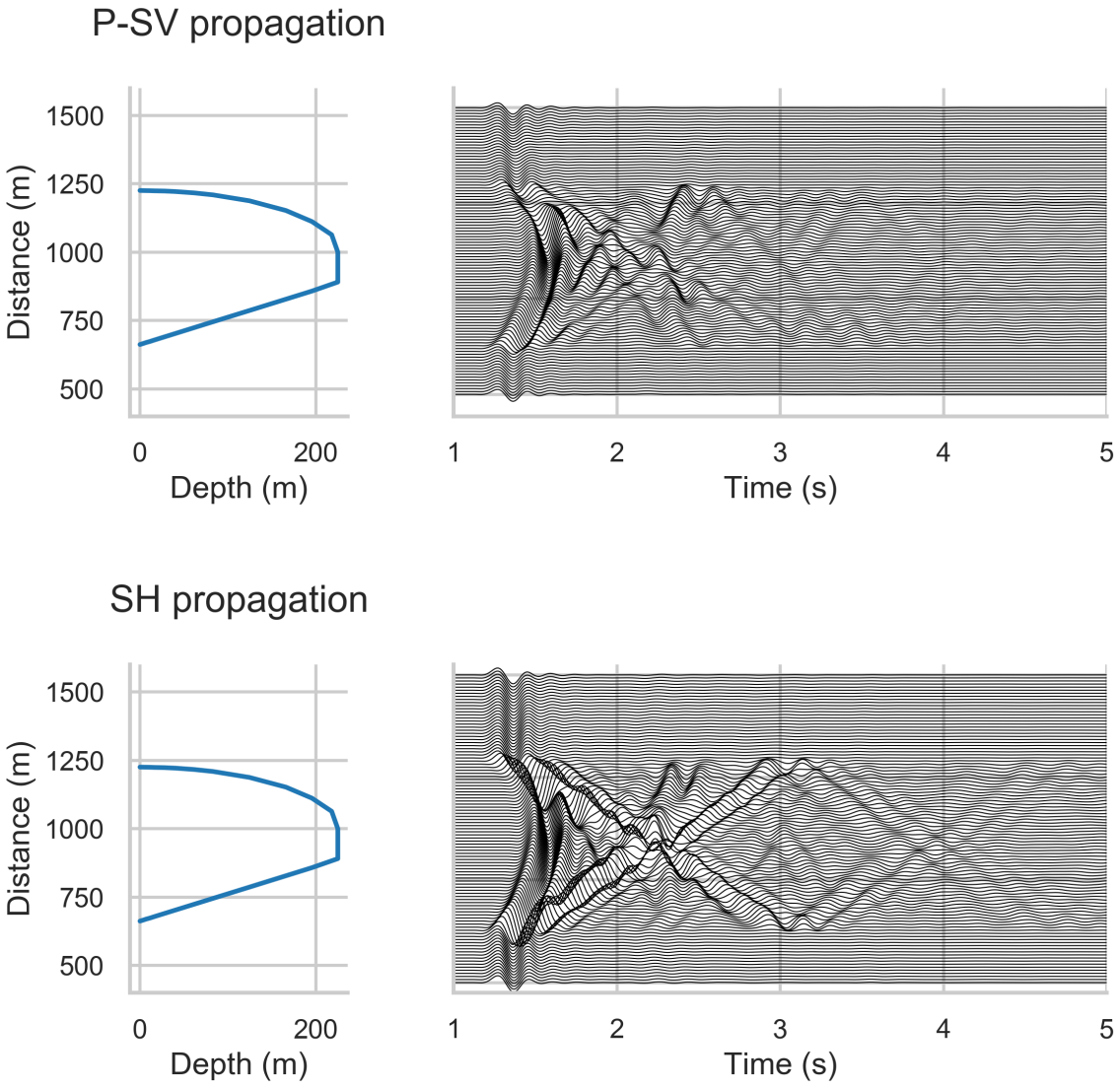

Figure 4: Horizontal components of the particle velocity at the free surface of the P-SV model (top) and SH model (bottom) for viscoelastic wave propagation in the 2D basin model subject to an input motion of PGA 0.2 g. For reference, the profile of the basin is plotted (sideways) in the left panels.

In addition to the particle velocities, the spectral ratios are computed for the P-SV and SH wave propagation, Figure 5. The spectral ratios are computed as the ratio of FFT values of basin signals to the geometric mean of bedrock signals. The fundamental frequency corresponds to 1.25 Hz and 1 Hz for P-SV and SH wave propagation, respectively. The influence of the basin asymmetry on the P-SV wave propagation is evident from the spectral ratio values, which are higher close to the right basin boundary than to the left boundary. To a lesser extent, this asymmetric amplification is also apparent for the SH case.

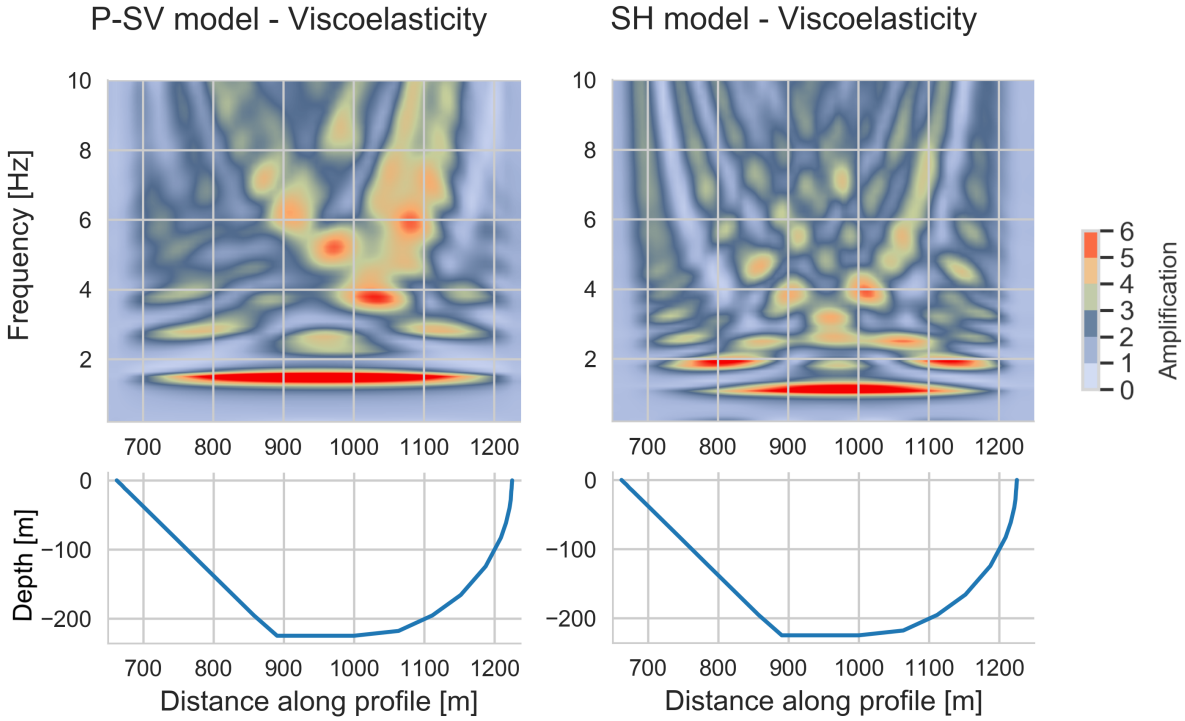

Figure 5: Spectral-ratio distribution of the viscoelastic surface motion for horizontal component of P-SV model (left) and SH model (right) on the frequency band 0.2-10 Hz. For reference, the profile of the basin is plotted in the lower panels.

We recall that the 2D resonance pattern is expected to dominate the SH wave propagation, as suggested by Bard and Bouchon (1985). To compare 1D and 2D natural frequencies, we computed the mean shear-wave velocity of basin soil, using the travel-time-based shear-wave velocity average as proposed by Roten et al. (2006). This value equals to 642.8 m/s and corresponds to a 1D fundamental frequency of 0.7 Hz. The calculated 2D fundamental resonance frequencies are notably greater than the 1D frequencies (greater by a factor 1.8 for SV waves and 1.4 for SH waves). This difference between 1D and 2D natural frequencies underlines the importance of the geometry effect on the basin response for both P-SV and SH

wave propagation.

Moreover, Bard and Bouchon (1985) demonstrated that SV waves resonate at higher frequencies than SH waves by a certain factor depending on the shape ratio of the propagation medium. In our case, the fundamental frequency for SH wave propagation is smaller than for the P-SV case, in accordance with Bard and Bouchon (1985). As a result, the distribution of spectral ratios within the basin is different for the two cases: amplifications globally appear at lower frequencies in the SH case than in the P-SV case. Slight amplifications are noted close to the right boundary for the frequencies above 2 Hz. Since the SH waves are out-of-plane and P-SV waves are in-plane, the reflections inside the basin are expected to be differently influenced by the basin geometry. Such a difference in wave propagation could explain the differences in the distribution of P-SV and SH models.

It is also known that the impedance contrast inside the basin can affect the resonance modes of SV and SH waves (Semblat et al., 2005; Ermert et al., 2014). To distinguish the effect of the impedance contrast from that of the basin geometry, we performed additional analyses (not shown here), where we simulated P-SV and SH wave propagation by assuming a single type of sedimentary soil inside basin. The shear wave velocity was set to the mean shear velocity of the basin soil (642.8 m/s as aforementioned). The analyses showed that the homogeneous basin resonates at approximately 1.5 Hz and 1 Hz for P-SV and SH cases, respectively. The difference between the 1D (being 0.7 Hz) and 2D natural frequencies also persisted for homogeneous basin simulations, which highlights the importance of the effect of 2D geometry on P-SV and SH basin responses.

To investigate the ultimate deformation reached in the basin for each case (P-SV and SH models), we analyse the maximum shear strain, Figure 6 (top panels). This figure presents the maximum shear strain values normalised by the maximum value of shear strain of the P-SV model for each point of the basin. The maximum strain value over the entire basin is 0.022 % for the P-SV model, and it is slightly lower in the SH model (0.019 %). The highest values are concentrated in the upper layers down to GL-50 m. The location where the maximum strain is calculated is marked by a star. This location is different for the P-SV and SH models: in the P-SV model it is close to the right boundary (x = 1050 m) at GL-11.5 m, while in the SH model it is close to the centre (x = 940 m) at GL-15 m. The values of maximum strain decrease for deeper layers in both models, and layering of maximum-strain patches is clearly seen. The presence of such discrete regions of strain inside the sediment layers can be attributed to the velocity contrast between each subsequent layer. Higher strain values are calculated close to layer boundaries. Such layering was also obtained by Gélis and Bonilla (2014), who showed that a gradually increasing velocity profile produces a slightly smoother strain distribution. A similar result of elevated strain values at layer boundaries was also reported by Gandomzadeh (2011) for a 2D nonlinear model of the Nice basin (France).

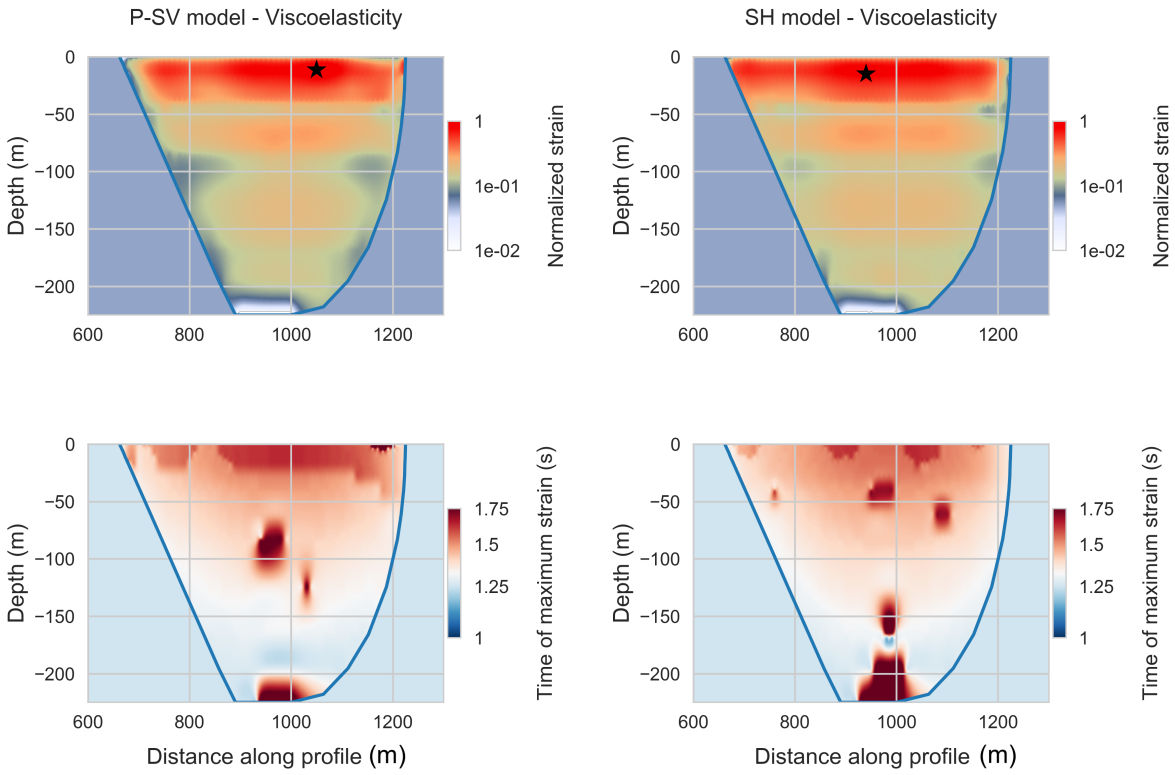

Figure 6: Maximum-strain (top) and trigger-time (bottom) distribution of the P-SV model (left) and the SH model (right) for viscoelasticity. The locations of maximum strain values are indicated by a star.

The instant at which the maximum strain is reached is also computed (bottom panels of Figure 6). In both models, the maximum-strain values in superficial layers are generally reached before 1.75 s. This indicates that the highest strain values in upper layers are triggered by the incidence of the strongest part of the input motion (between 1 - 1.5 s as shown in Figure 4). Incident waves reflected back from the free surface towards the basin bottom (after 1.75 s) increase the degree of deformation reached at the bottom of the basin near the bedrock interface, even though the maximum strain in these layers is relatively low. We observe an overall tendency of the strain to increase towards the surface, and that the high values of strain result from the strongest part of the incident waves inside the basin.

3.3.2 Nonlinear response of the 2D basin model

We analyse the nonlinear response of the basin with and without consideration of excess-pore pressure development for P-SV and SH wave propagation types. The input motion is the same as in the viscoelastic case (Figure 3). First, we analyse the nonlinear surface motion in the P-SV and SH models. Figure 7 shows the wavefield velocity of the horizontal components at the free surface of the P-SV model (top) and the SH model (bottom) for the nonlinear soil response with no pore-pressure effects. The amplitude of the basin waves is strongly attenuated in both models due to nonlinearity. The propagation of the basin waves travelling from one basin margin to the other is attenuated. The strongest part of the input motion is present in the beginning of the signal. Hence, the nonlinearity-related effects are triggered from the

beginning of propagation. However, the energy content of realistic input motions is rather complex in both the time and frequency domains (Gélis and Bonilla, 2012), and the strongest part of the ground motion does not correspond to first arrivals. Such complexity of input motion may exert different controls on ground motion by continuous changes in loading/unloading cycles. We reserve this aspect for future studies. Instead, we concentrate on the effect of the nonlinear response on wave propagation, which warrants the use of a simple signal to isolate this phenomenon.

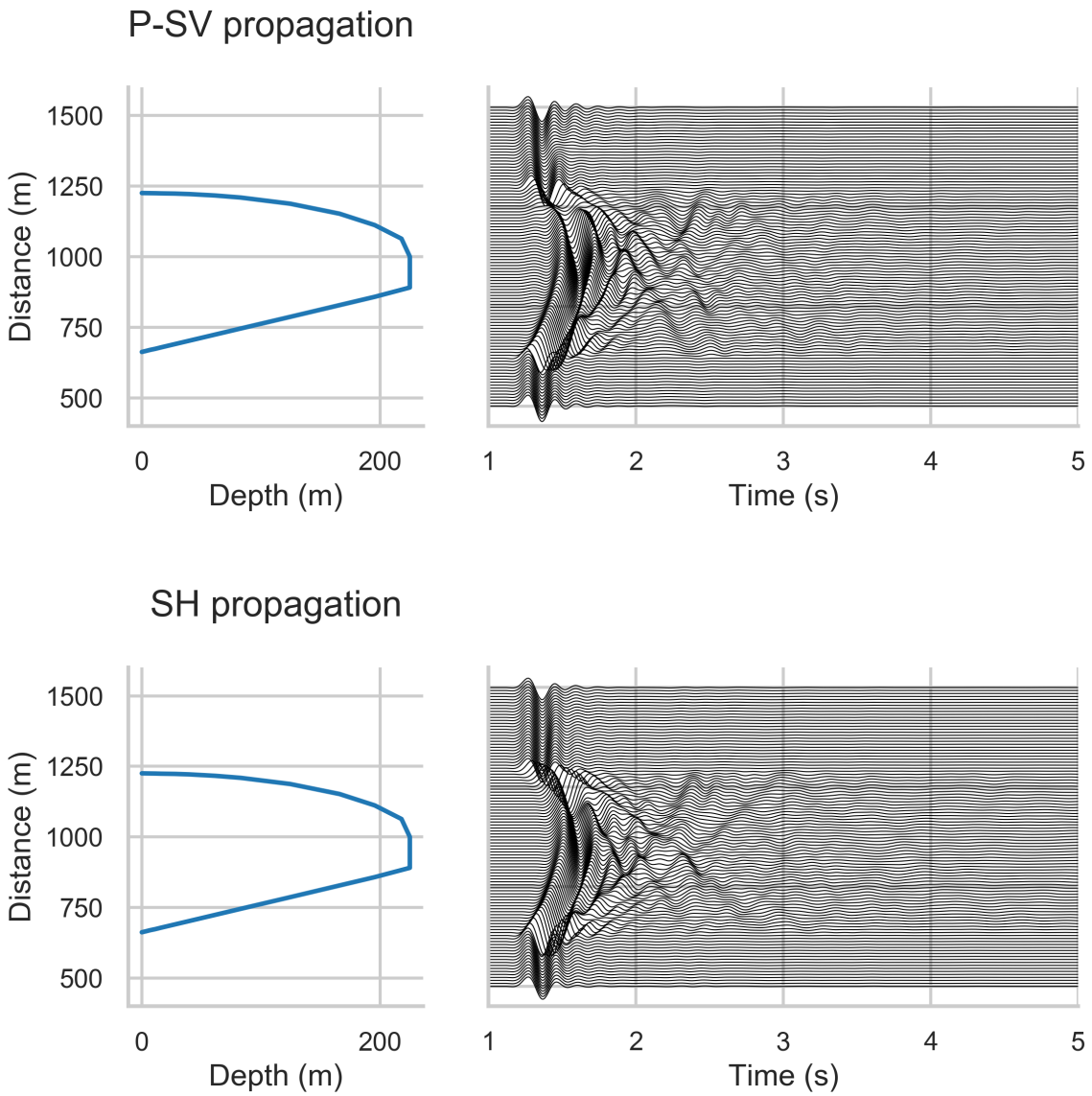

Figure 7: Horizontal components of the particle velocity at the free surface of the P-SV model (top) and SH model (bottom) for the nonlinear model without pore-pressure effects in the 2D basin model in response to the input motion of PGA 0.2 g. For reference, the profile of the basin is plotted (sideways) in the left panels.

We compare velocity-time histories and their Fourier amplitude at the basin and bedrock surface for the P-SV and SH models. The basin signal is chosen at a position of x=1100 m from

the left boundary, and the bedrock signal is represented by the geometric mean of all bedrock stations (Figure 8). We first make the comparison for the nonlinear basin in the absence of pore-pressure effects. The waves refracted from the basin into the bedrock are different in the P-SV and SH cases, and therefore slight amplification in the wave and Fourier amplitudes in the bedrock (black lines) is observed in the SH model as compared to the P-SV model. Similar to the linear case, the amplitudes of both the P-SV and SH basin waves are greater than those of bedrock, and the duration of propagation is longer inside the basin. Waves are amplified in the whole frequency band inside the basin, and the waveform and energy content of P-SV and SH waves inside the basin are different. Recall that P-SV and SH wave propagation of the vertically incident horizontal wave field would be identical in a medium where no horizontal variation of soil layer exists. Here the 2D basin shape promotes differences in P-SV and SH wave propagation, since the formation of P waves due to the basin geometry is not present in the SH model. We also note that the Fourier amplitude of the calculated ground motion of both the basin and bedrock decreases beyond 8 Hz, reflecting the limited energy contained in the source.

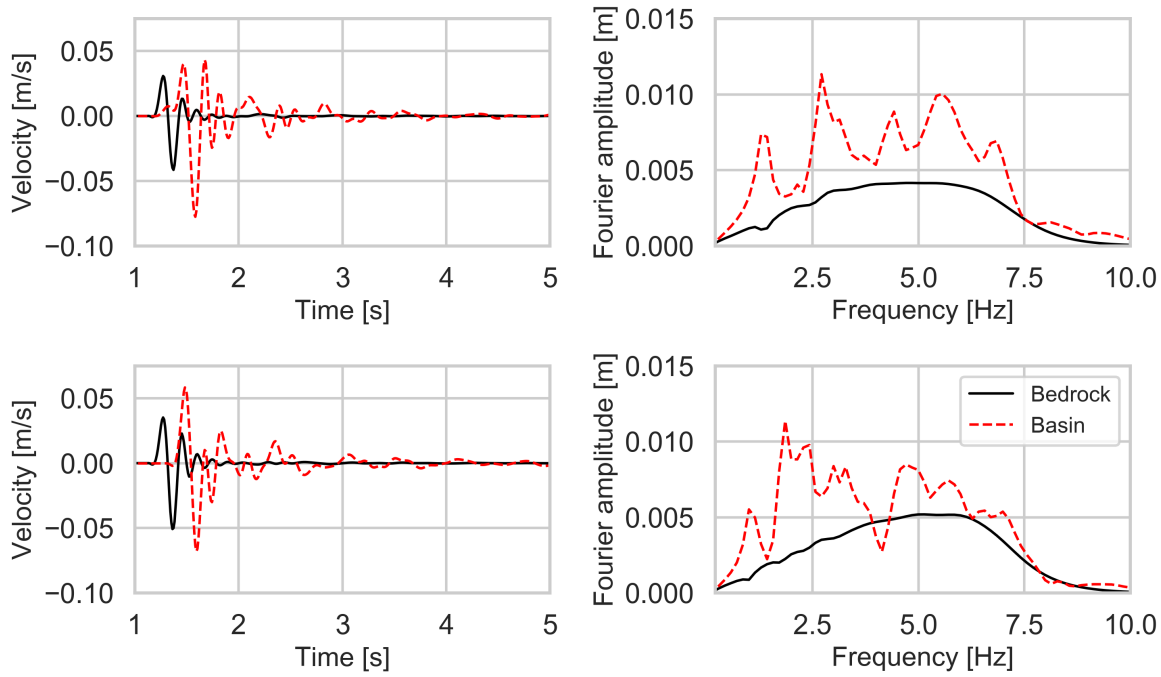

Figure 8: Velocity-time histories (left) and Fourier amplitude (right) of the bedrock (solid black lines) and the basin (dashed red lines) for the nonlinear model without pore-pressure effects (total stress analysis) of P-SV (top) and SH (bottom) propagation models.

Next, we make a comparison between the surface motion of the basin and bedrock for nonlinearity with pore-pressure effects. Again both the P-SV and SH models are analysed (Figure 9). The waveform and spectral shape of the nonlinear basin response is preserved also under the effect of excess-pore pressure development for both the P-SV and SH models. Slight changes in velocity amplitudes and the peaks of Fourier amplitudes are observed as a result of pore-pressure effects.

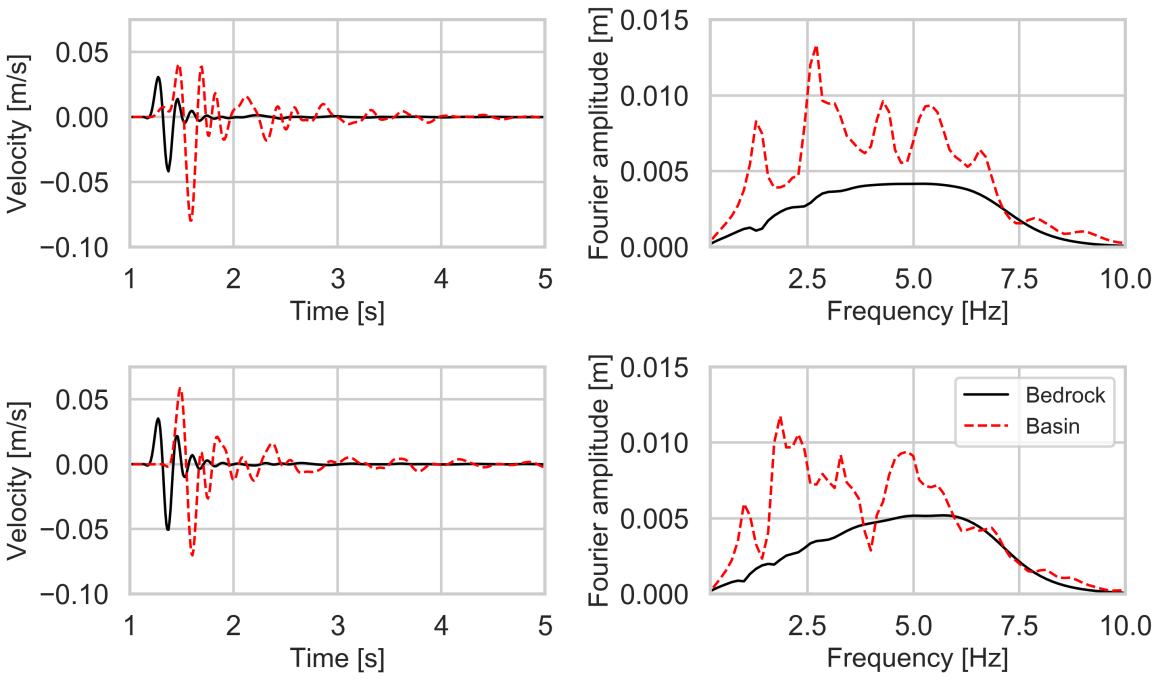

Figure 9: Velocity-time histories (left) and Fourier amplitude (right) of the bedrock (solid black lines) and the basin (dashed red lines) for the nonlinear model with pore-pressure effects (effective stress analysis) of P-SV (top) and SH (bottom) propagation models.

Previous studies (e.g. Roten et al., 2012; Martino et al., 2015) have demonstrated that soil nonlinearity influences wave propagation by signal damping, particularly at high frequencies, and causes a shift in resonance frequencies towards lower values. In Gélis and Bonilla (2014), such nonlinearity effects are shown to be dependent on the spectral content of the input signal. In their study, a global diminution of spectral-ratio amplitudes is observed when the basin is affected by nonlinear effects even under a simple impulse Gabor signal. In the same study, the nonlinear basin response under a real input motion exhibits an amplified high-frequency content. Such an amplification has been attributed to the low values of Fourier amplitudes at the corresponding frequencies. Here, the energy content of the source is relatively weak at high frequencies (> 8 Hz), as compared to the rest of the frequency band. Thus, the following analyses are performed up to 8 Hz where the source energy is sufficiently high.

To compare the spectral-ratio amplitudes at the whole basin surface for the viscoelastic and nonlinear propagation media, we analyse transfer functions. Figure 10 shows this comparison for viscoelasticity (left) and nonlinearity without pore-pressure effects (total stress analysis; middle). We note that the basin nonlinearity without pore-pressure effects results in attenuation of spectral ratios at intermediate frequencies (> 2 Hz) in both P-SV and SH models. The natural frequency of the basin is shifted slightly to lower values compared to viscoelasticity: it is reduced from 1.25 to 1.15 Hz for the P-SV case and from 1 to 0.85 Hz for the SH model, respectively. It is worth noting that the distribution of the nonlinear P-SV and SH models are still similar to the viscoelastic models.

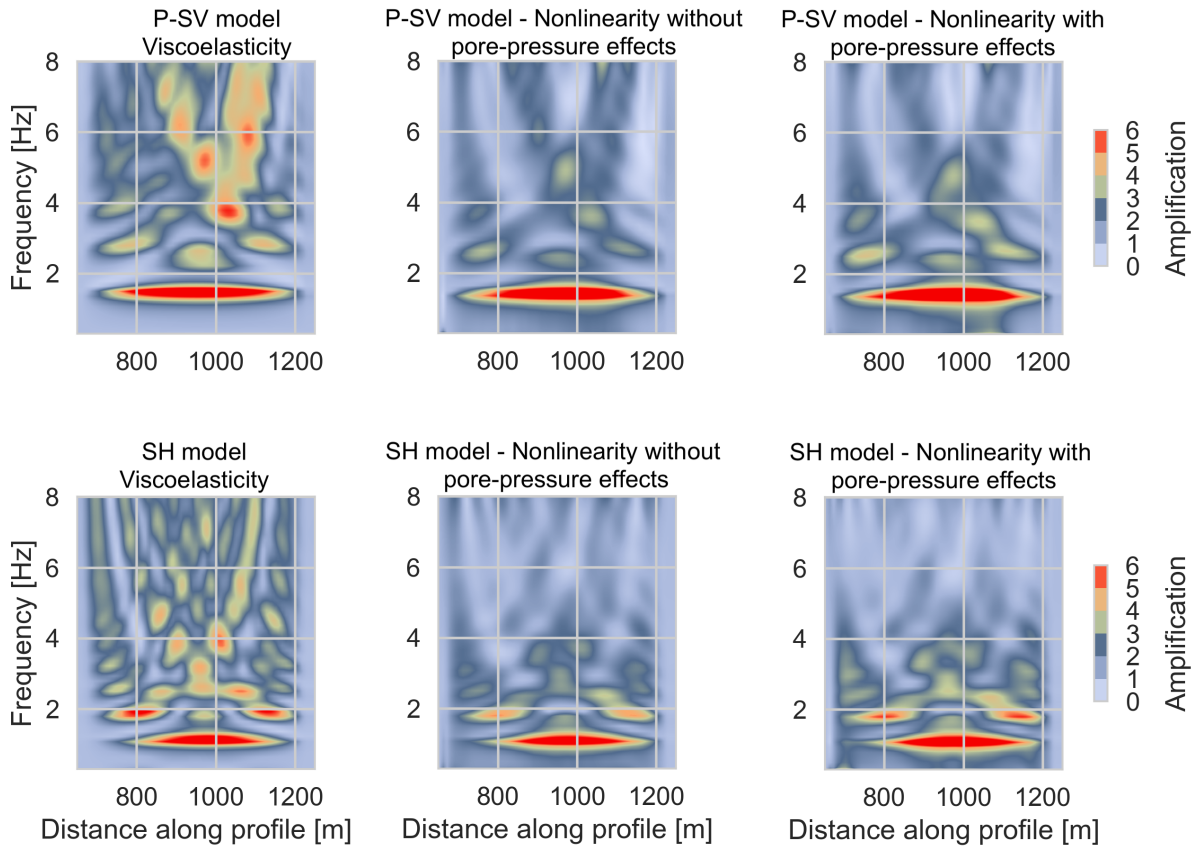

Figure 10: Spectral-ratio distribution of the surface-motion for the horizontal component of the P-SV model (top panel) and SH model (bottom panel) for the viscoelastic model (left), the nonlinear model without pore-pressure effects (total stress analysis; middle), and the nonlinear model with pore-pressure effects (effective stress analysis; right).

To analyse the effect of excess-pore pressure development on the basin response, the transfer function for nonlinearity with pore-pressure effects (effective stress analysis) is also computed (right panels in Figure 10). Compared to the total stress analysis, a slight influence attributed to pore-pressure effects is observed in the amplification of spectral ratios at low frequencies (< 4 Hz), which is mostly pronounced at the basin margins. At high frequencies (> 4 Hz), pore-pressure effects cause damping of the ground motion as compared to the total stress analysis.

Like in the total stress analysis, we inspect the distribution of the maximum strain achieved in the basin for the P-SV and SH models in the effective stress analysis, for which the triggered nonlinearity level is higher due to pore-pressure effects. Figure 11 (top) displays the maximum-strain distributions in the basin for the P-SV (top) and SH (bottom) models. As before, the strain values are normalised by the maximum value of the SH model. The maximum strain value over the entire basin is 0.045 % for the SH model, and it is marginally higher than for the P-SV model (0.044 %). These values are approximately twice that of the viscoelastic case. Maximum deformation in viscoelastic case is reached for the P-SV case, whereas it is reached for the SH model in nonlinear case. By contrast, the differences between the two nonlinear models (P-SV and SH models) are minor. The highest values of strain are concentrated in highly superficial layers where the soil is the most nonlinear and

excess-pore pressure development occurs. In particular, the central part of the basin and the basin margins experience higher strains than the rest of the basin. Although the maximum strain values of P-SV and SH models are close, the location of these points is different similar to the viscoelastic case: It remains in the centre of the basin for the P-SV model (x = 1060 m) at GL-6 m and is shifted towards the left margin of the basin in the SH model (x = 690 m) at GL-6 m. Further analysis reveals that the maximum strain of the nonlinear basin without pore-pressure effects equals roughly 0.024 % for both the P-SV and SH models, being very close to the viscoelastic case, and also its lateral position is the same as in the viscoelastic case. However, this location is shifted to shallower depths due to nonlinearity (from GL-8 m to GL-6 m for the P-SV case and from GL-11.5 m to GL-6 m for the SH case). Such a shift effect is also noted under pore-pressure effects: as the basin becomes more nonlinear, the location of maximum strain is shifted further to shallower depths.

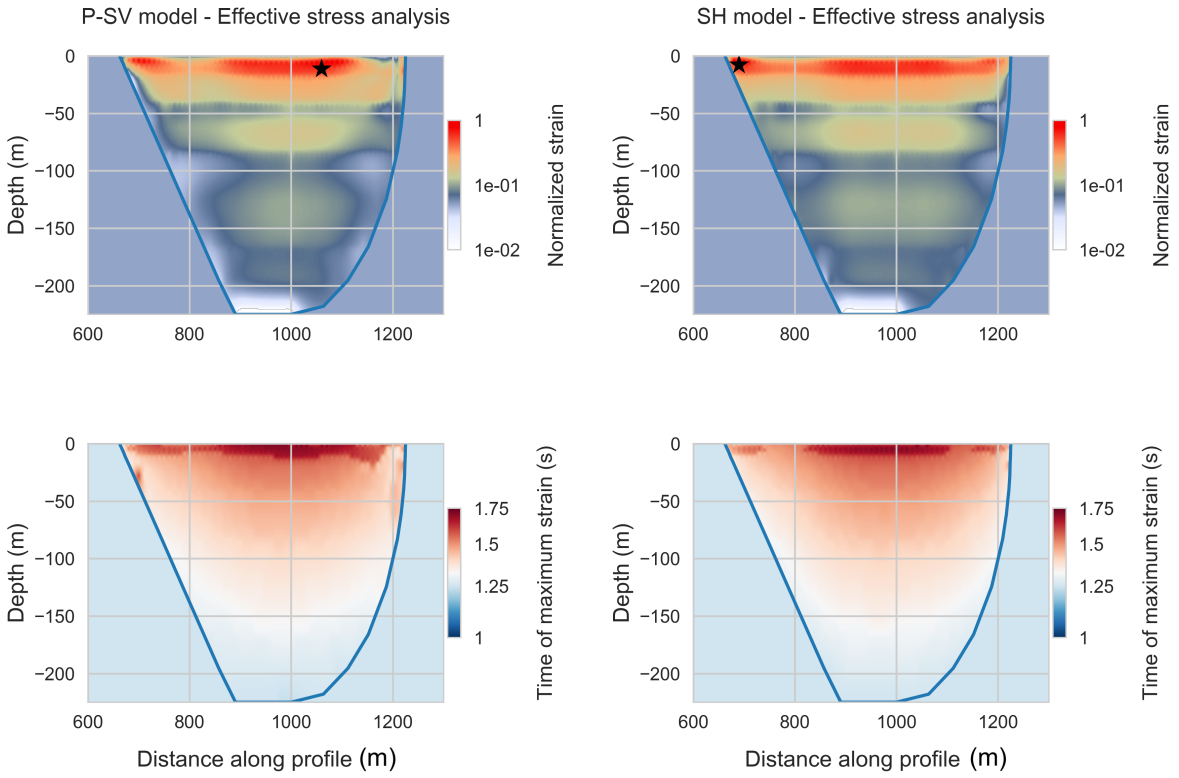

Figure 11: Maximum-strain (top) and trigger-time (bottom) distribution of the P-SV model (left) and SH model (right) for nonlinearity with pore-pressure effects. The locations of the maximum-strain values are indicated by a star.

Regarding the triggering-time distribution of the maximum-strain values (bottom panels in Figure 11), the basin becomes nonlinear within 1.5 s. Similarly to the viscoelastic case, the maximum deformation is attributed to the strongest ground motion for superficial layers. Yet, small patches of maximum strain induced by later wave arrivals, as seen in the viscoelastic case, are not present here. Furthermore, we verified that the triggering-time distribution of maximum-strain values is very similar for both nonlinearity cases with and without pore-pressure effects. Thus, the absence of small patches of enhanced deformation could be related

to the damping caused by nonlinearity.

Gélis and Bonilla (2014) concluded that maximum shear strain reaches higher values in superficial layers than in underlying layers. This localisation effect is even more pronounced in the present study, owing to the pressure dependency of nonlinearity and the pore-pressure effects which reduce the soil strength near the surface. Because of the same effects, the contrast between the strain level in the various basin layers is enhanced compared to the viscoelastic case. We also observe higher strain values close to the basin margins, in particular close to the left boundary that is more steeply inclined than the right boundary. Such a finding is in agreement with Guidotti et al. (2011) who considered different combinations of model geometry and material properties in 2D trapezoidal models, subjected to vertically propagating SV waves. They showed that the 2D nonlinear valley response is highly dependent on the basin geometry, and it is mostly pronounced close to the basin margins.

Next, we analyse the differences between total and effective stress computations by displaying the stress-strain curves, for both P-SV and SH cases with and without pore-pressure effects (left panels in Figure 12. The stress-strain curves are obtained from the middle of the first layer (top) and the middle of the second layer (bottom panel) at the centre of the basin at x = 1060 m, where strong nonlinear effects have been computed (Figure 11). Comparison of stress-strain curves between the simulations with and without pore-pressure effects reveals similar resultant behaviour in layer 1 and layer 2. In both layers, increased nonlinearity level due to pore-pressure effects causes strain increase and strength weakening as the shear modulus (slope of stress-strain curve) is lowered owing to the rise of pore-pressure excess. The difference between total and effective stress analyses is more pronounced for layer 1. The triggered nonlinearity is comparatively small, taking into account that the maximum deformation is less than 0.1%, and only minor differences in stress-strain curves result from pore-pressure effects.

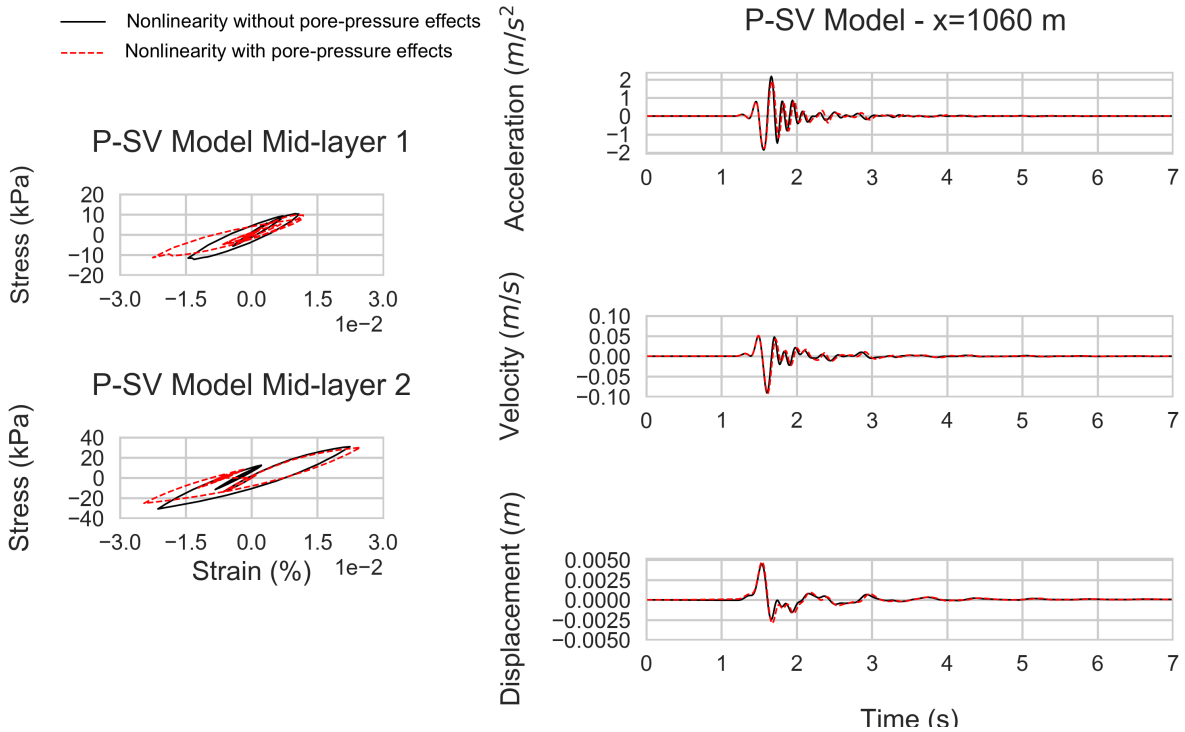

Figure 12: Comparison of stress-strain curves (left) at GL-3.5 m (top panels) and GL-11.5 m (bottom panel) and comparison of time histories (right) of surface-acceleration (top panel), velocity (middle panel), and displacement (bottom panel) between effective (dashed lines) and total (solid lines) stress analyses in the P-SV model.

The same comparison as for the P-SV model is presented in Figure 13 for the SH model. The stress-strain data are obtained from the top two layers at a point located in the left section of the basin at x = 690 m, where the highest strain is computed. Similar to the P-SV model, pore-pressure effects manifest themselves in elevated strain and in strength loss, which is particularly apparent in the first layer. Owing to the higher degree of nonlinearity compared to the P-SV model, the maximum strain values are greater in the SH model than in the P-SV model (for example, 0.023 % in P-SV model and 0.035 % in SH model for layer 1). However, these differences are rather small given the limited degree of triggered nonlinearity.

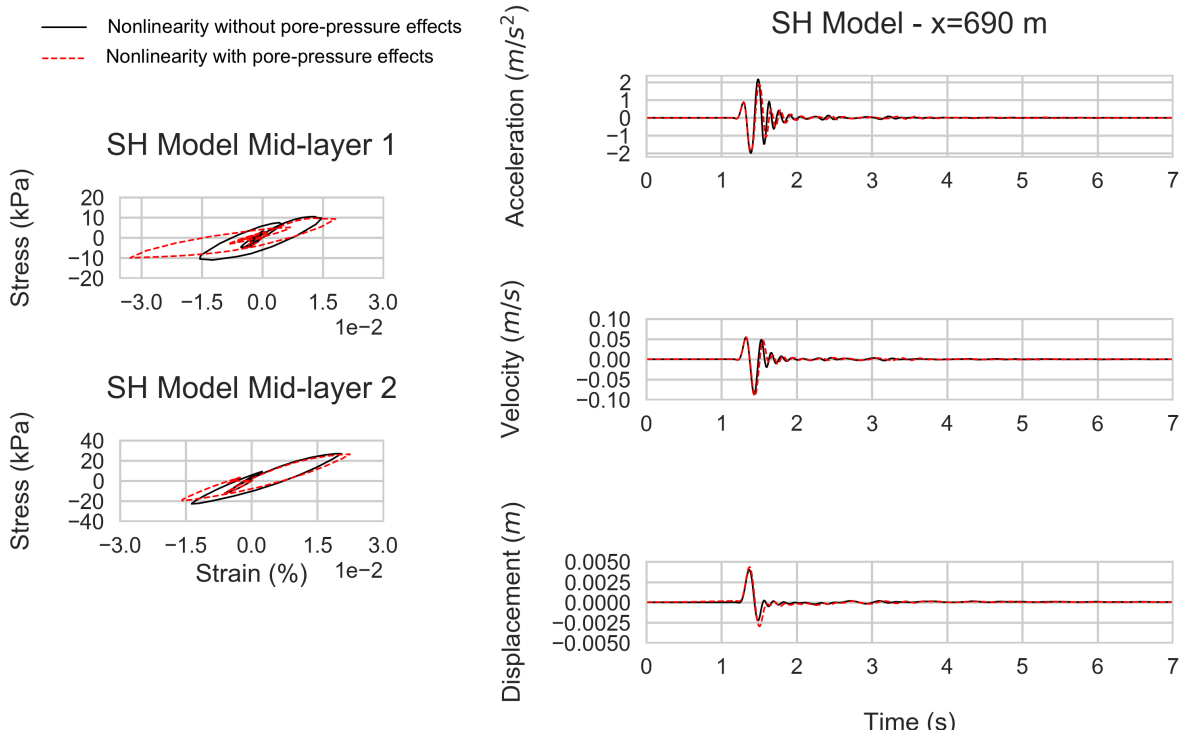

Figure 13: Comparison of stress-strain curves (left) at GL-3.5 m (top panel) and GL-11.5 m (bottom panel) and comparison of time histories (right) of surface-acceleration (top panel), velocity (middle panel), and displacement (bottom panel) between effective (dashed lines) and total (solid lines) stress analyses in the SH model.

Surface-acceleration, velocity, and displacement time histories for the total and effective stress analyses of P-SV and SH models are also compared, as presented in the right panels of Figure 12 and Figure 13, respectively. Waveforms of the P-SV and SH models diverge after 1.5 s: amplitudes of oscillations are amplified in the P-SV model compared to the SH model. This is similarly seen in the results of the two models when considering the differences between the total and effective stress analyses. Pore-pressure effects lead to slight damping in amplitude

before 2 seconds, and waves exhibit a slight phase shift. Peak ground acceleration (PGA) is approximately 2 m/s^2, peak ground velocity (PGV) is 0.095 m/s, and maximum displacement is 0.48 cm for both approaches. Similar to the stress-strain curves, pore-pressure effects on surface-motion time histories are not substantial either. Such an outcome could be attributed to the small degree of deformation that the soil experiences under the imposed loading condition, acknowledging the simplicity of the input motion in terms of its loading/unloading history.

We also verified that these findings (nonlinear effects in P-SV and SH models) are stable after changing liquefaction-related parameters for the first two layers. Details of this analysis can be found in Supplementary Appendix B2.

3.3.3 Comparison of nonlinear basin response of 1D and 2D approaches

In the following section, we explore the effect of two-dimensional structure of the basin on soil nonlinearity by comparing 1D and 2D model results for two different locations within the basin, adopting the nonlinear soil constitutive model with pore-pressure effects. Results are shown for the SH model since the observed basin nonlinearity is higher for the SH model than for the P-SV model. We perform the simulations with the 1D-3C SEM code of Oral et al. (2017) for 1D modelling using the 1D soil properties at the left (x = 690 m) and central (x = 1060 m) parts of the basin at GL-6 m. The choice for these locations inside the basin is made based on the results of Section 3.3.2. The first location corresponds to the basin margin, and the second location to the centre of the basin. The sediment-bedrock interface is defined at GL-27.35 m and GL-225 m for the first and second locations, respectively. The input motion is as shown in Figure 3.

Time histories of acceleration (top), velocity (middle), and displacement (bottom) for the left section (left panels) and the central section (right panels) are compared between the 1D and 2D models in Figure 14. Beyond 2 seconds of wave propagation, motion is seen to be attenuated in 1D, while the SH waves inside the 2D basin still propagate until the end of the simulation. Our additional tests on 1D and 2D models indicate that the 2D geometry results in an amplified and extended wave propagation within the basin (at both locations) in the linear case (see Supplementary Appendix C). The wave propagation in 2D remains complex compared to 1D, also when considering the soil nonlinearity, as illustrated by the continuous reflections and the amplitude differences between the 1D and 2D results. The strongest motion is at 1.5 s, and the PGA at both sections is greater in 2D than in 1D (approximately 1.5 m/s^2 in 1D; 2 m/s^2 in 2D at the left section and slightly weaker in the centre of the basin). In displacement-time histories, longer durations of ground motion are observed in the 2D model in both sections, while the strongest displacement is damped after the first peak in 1D. This aspect is seen clearly in the centre of the basin.

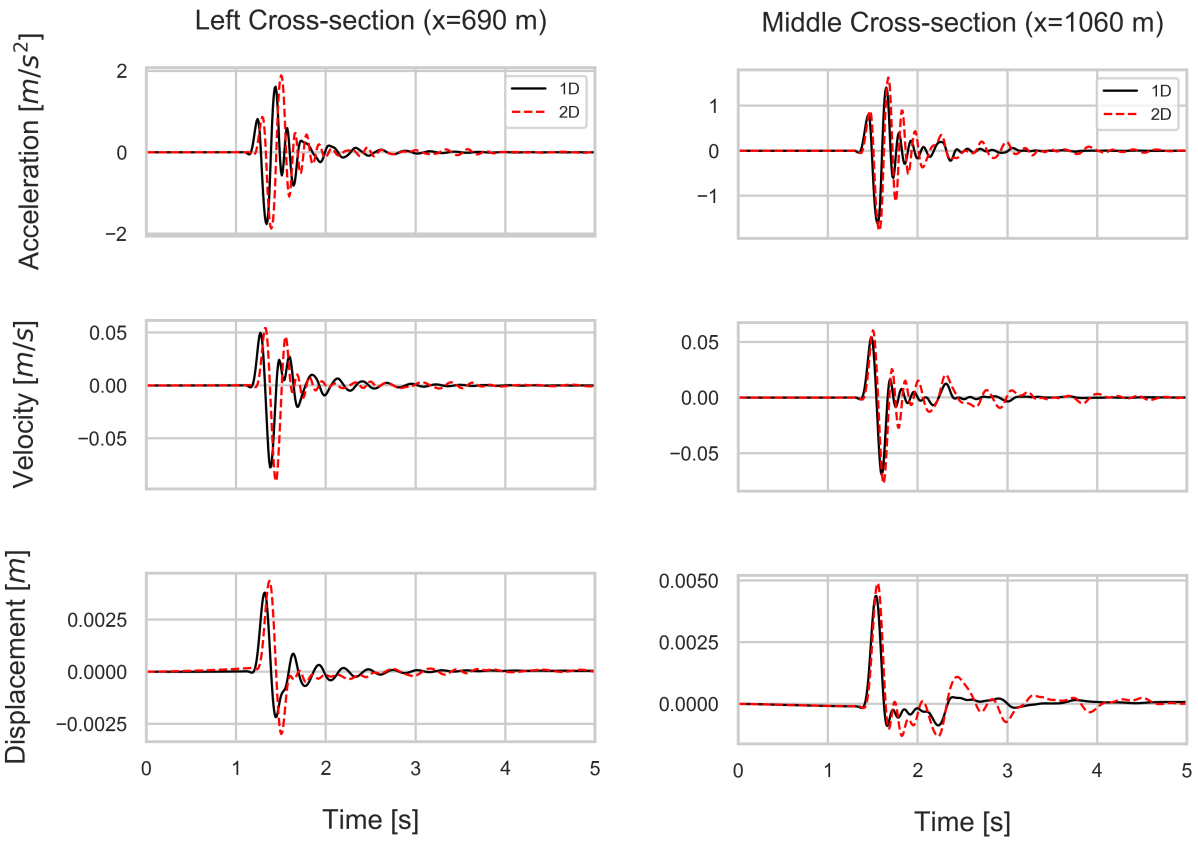

Figure 14: Comparison of time histories of surface acceleration (top panel), velocity (middle panel) and displacement (bottom panel) between 1D (solid lines) and 2D (dashed lines) approaches for the left column (left) and central column (right) for nonlinearity with pore-pressure effects.

Figure 15 displays the comparison of the 1D and 2D Fourier amplitudes of the surface velocities for the two locations. The signal content in the left section displays a resonance peak at around 3 Hz, attributed to the thin sedimentary layer resonance. The frequency content of the 2D motion at the same section is slightly shifted towards higher frequencies with consistently higher fundamental resonance frequencies in this 2D model than in the corresponding 1D model (see the discussion in Section 3.3.1). In the central section, the shape of the Fourier amplitudes of the 1D and 2D approaches are similar. However, 2D amplification is slightly shifted towards higher frequencies compared to that in 1D. The wave propagation in the 2D model produces significant amplification over the whole frequency band.

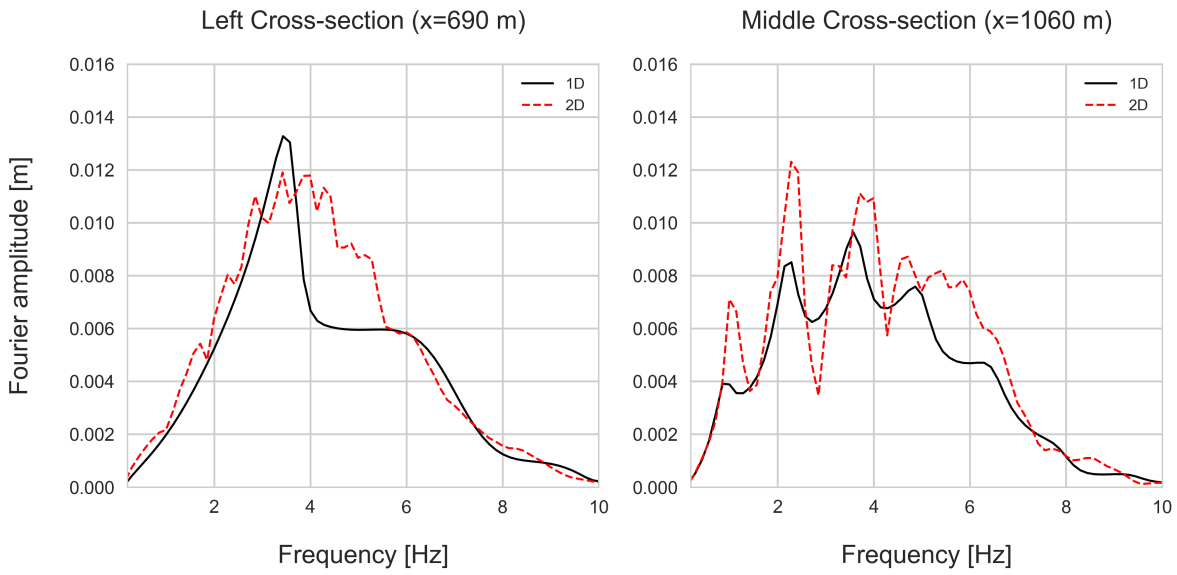

Figure 15: Comparison of Fourier amplitudes of the surface velocities between 1D (solid lines) and 2D (dashed lines) approaches for the left column (left) and central column (right) of the basin model for nonlinearity with pore-pressure effects.

To compare the nonlinearity levels of 1D and 2D models, we further analyse the stress-strain curves, deviatoric plan and excess-pore pressure development. Figure 16 displays this comparison for the left location (left) and the central location (right) inside the basin. Deviatoric plan quantifies the change in effective stress of liquefiable soil under applied shearing. Deviatoric stress and effective stress values are normalised by the initial effective mean stress. This normalisation is also applied to pore-pressure excess values. In the stress-strain diagram of the left column, soil experiences approximately 4.5 times larger deformation in the 2D model (0.045 %) than in the 1D model (0.01 %). For the central column, a similar difference is seen between the 1D and 2D models with slightly lower values of strain (approximately 4 times more strain in 2D than 1D). Higher strength loss is apparent from the lower stress-strain tangent in the 2D results of both sections, as compared to 1D. These results indicate that the level of nonlinearity triggered in the 2D model is higher than in 1D. The amplifications of ground motion in the 2D model enhance the basin nonlinearity. The increase in nonlinearity is also seen in the decrease of effective stress values. In both sections, the initial soil strength is reduced to its half in the 2D model, whereas it is limited to a decrease of 15 % and 10 % for the left and central sections, respectively, in the 1D model. Such a decrease in effective stress values results from the rise of pore-pressure excess. The 2D soil nonlinearity is shown to induce excess-pore pressure development of more than 50 % at both columns. Soil nonlinearity is relatively low in 1D so that the pore-pressure excess is less than 15 % at both sections. We note that the complex wave propagation triggers more nonlinearity and accordingly enhances the pore-pressure level in the 2D model compared to the 1D case.

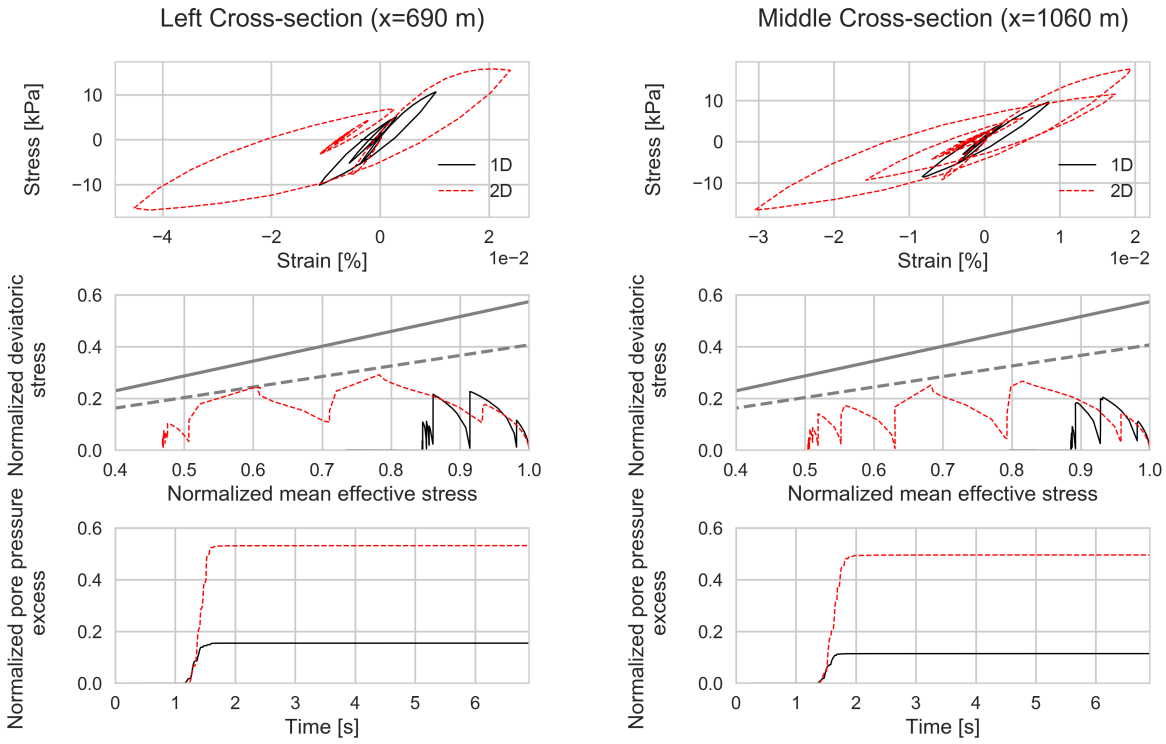

Figure 16: Comparison of stress-strain curves (top panel), deviatoric plan (middle panel) and temporal change of pore-pressure excess (bottom panel) between 1D (solid lines) and 2D (dashed lines) approaches for the left column (left) and central column (right) for nonlinearity with pore-pressure effects. Failure and phase transformation lines are indicated by grey solid and dashed lines (in gray), respectively, in the deviatoric plans shown in the middle panels.

These results demonstrate that the combined effect of the 2D geometry and the soil nonlinearity results in a more complex wave propagation in 2D as compared to 1D. Higher wave amplitudes and extended wave propagation due to the 2D effects enhance the pore-pressure excess and trigger additional nonlinearity. This effect of the dimensionality on nonlinear basin response is clearly seen even though the maximum strain is only modest (< 0.1 %). On the other hand, Fourier spectra, and therefore amplification functions with respect to the linear bedrock, are still higher in 2D than in 1D in some frequency bands. Thus, taking into account the 2D-geometry effects has great importance for modelling seismic wave propagation both in linear and nonlinear media.

4 Conclusions and Perspectives

The 1D-3C spectral element modelling in Oral et al. (2017) has been extended to 2D for modelling the nonlinear soil response with pore-pressure effects in multi-dimensional media. The MPII model of Iwan (1967) and liquefaction front model of Iai et al. (1990) are implemented to SEM2DPACK software, and verification of the implementation of new features is performed. The code is suitable for studying the effects of various physical processes, such as attenuation

and nonlinear material behaviour including pore-pressure effects on the ground motion.

The extended numerical model has been applied to a two-dimensional sedimentary basin model to study the effect of soil nonlinearity on wave propagation in complex media. The 2D basin model consists of six soft layers situated within a basin surrounded by bedrock. Basin and bedrock are separated on one side by an elliptical boundary and on the other side by a boundary with a steeper inclination, introducing complexity in the wave propagation in the model owing to the asymmetry of the basin geometry. Two superficial soil layers are dictated to be susceptible to excess-pore pressure development, and we performed nonlinear analyses with and without pore-pressure effects using a truncated Gaussian signal with a free surface PGA of 0.20 g in the in-plane (P-SV) and out-of-plane (SH) wave propagation models. We found that :

a) Nonlinear basin response is sensitive to the differences in P-SV and SH waves propagation. As expected, the 2D basin geometry results in interference of basin-edge generated waves and vertically propagating waves and, hence induces differences in P-SV and SH wave propagation. The basin response in the P-SV and SH models remains different also under nonlinear effects.

b) The excess-pore pressure development in shallow layers triggers more nonlinearity, and it causes additional strength loss and deformation in these layers. Therefore, pore-pressure effects increase the strain contrast between superficial layers and the rest of the basin. Moreover, the asymmetric basin geometry results in spatial variability of such nonlinear effect: patches with relatively high strain values in shallow layers are computed, in particular at the centre of the basin and close to basin margins.

c) The energy of ground motion is damped in the whole frequency band (at frequencies below 8 Hz where the energy content of the source is relatively high) when considering nonlinearity without pore-pressure effects. Some of the past studies point to the amplification of low-frequency content of surface motion due to significant excess-pore pressure development (e.g. Laurendeau et al., 2017; Oral et al., 2017). Yet, such notable pore-pressure related effects are not found in surface motion (such as time histories of acceleration, velocity and displacement) in this case where a simple wavelet is used as input motion. Exploring this aspect under different input motion needs further study. Studying the changes in triggered nonlinearity level under realistic input motion with a complex energy content is a critical topic for future investigations.

d) As already known for linear soil response, the 2D basin geometry results in amplification of wave amplitudes and increase of duration of wave propagation with respect to 1D. A complex wave propagation in 2D modelling brings higher nonlinearity all over the basin compared to 1D modelling. High degrees of nonlinearity in 2D modelling could lead to strength loss and pore-pressure rise that cannot be predicted from 1D modelling. Furthermore, amplification functions with respect to the linear bedrock are still higher in 2D than in 1D in some frequency bands. Thus, we recommend multi-dimensional modelling of wave propagation in seismic hazard assessment studies for nonlinear complex media.

This numerical study aims at better understanding the physics and the key parameters governing the 2D nonlinear wave propagation. Our results highlight the importance of considering 2D geometry and soil nonlinearity and are stable for different soil conditions (as verified after a sensitivity study on the effect of liquefaction-related parameters). One can expect similar

results for comparison of 2D vs 3D modelling. Moreover, we recall that the source in this study is defined as a vertically incident wave field, which is warranted under the assumption that the model domain is positioned sufficiently far from fault, i.e. for far-field ground-motion modelling. In the near-field region, source properties and its rupture process become significant factors to account for in seismic hazard studies. Certain studies successfully model 3D near-field ground motion including the causative fault itself assuming linear media or nonlinear media for a limited frequency band (e.g. Stupazzini et al., 2009; Oral et al., 2018). Improving the knowledge of nonlinear effects on ground motion under rather simplified conditions of input and geometry (2D vs 3D), as scoped in this study, is helpful prior to real case scenarios (such as studying near-field broadband ground-motion in 3D nonlinear media). In that sense, our study constitutes a sensitivity analysis preliminary to comprehensive real-case studies. The extension of our analyses on a real basin and also considering near-field input conditions are future perspectives.

Data and resources

The numerical tool for 2D spectral-element wave propagation modelling (version 2.3.8) is available at `https://github.com/jpampuero/sem2dpack` address. All the updates can be followed on the same address.

Acknowledgements

The authors would like to thank Harsha S. Bhat, Jean-Paul Ampuero and Marion Thomas for their collaboration and helpful comments in using SEM2DPACK for multi-dimensional modelling of seismic wave propagation in nonlinear media, to Elise Delavaud for her assistance in the preparation of this work, and to Martijn van den Ende for his final touch to enrich the readability of the manuscript.

We furthermore acknowledge the comments of the Editor René-Edouard Plessix and two anonymous reviewers, which definitely improved the quality of the manuscript.

References

Aguirre, J. & Irikura, K. (1997), 'Nonlinearity, liquefaction, and velocity variation of soft soil layers in port island, kobe, during the hyogo-ken nanbu earthquake', *Bulletin of the Seismological Society of America* **87**, 1244–1258.

Ampuero, J.-P. (2002), Etude physique et numérique de la nucléation des séismes, PhD thesis, Paris 7.

Assimaki, D., Li, W. & Kalos, A. (2011), 'A wavelet-based seismogram inversion algorithm for the in-situ characterization', *Pure and applied geophysics* **168**(10), 1669–1691.

Bakir, B. S., Sucuoglu, H. & Yilmaz, T. (2002), 'An overview of local site effects and the associated building damage in adapazari during the 17 august 1999 izmit earthquake', *Bulletin of the Seismological Society of America* **92**(1), 509–526.

Bard, P.-Y. & Bouchon, M. (1985), 'The two-dimensional resonance of sediment-filled valleys', *Bulletin of the Seismological Society of America* **75**(2), 519–541.

Beyreuther, M., Barsch, R., Krischer, L., Megies, T., Behr, Y. & Wassermann, J. (2010), 'Obspy: A python toolbox for seismology', *Seismological Research Letters* **81**(3), 530–533.

Bonilla, L. F., Archuleta, R. J. & Lavallée (2005), 'Hysteretic and dilatant behavior of cohesionless soils and their effects on nonlinear site response: Field data observations and modeling', *Bulletin of the Seismological Society of America* **95**(6), 2373–2395.

Bonilla, L. F., Liu, P.-C. & Nielsen, S. (2006), 1d and 2d linear and nonlinear site response in the grenoble area, *in* 'Proc. 3rd Int. Symp. on the Effects of Surface Geology on Seismic Motion (ESG2006)'.

Bonilla, L. F., Tsuda, K., Régnier, J. & Laurendeau, A. (2011), 'Nonlinear site response evidence of k-net and kik-net records from the 2011 off the pacific coast of tohoku earthquake', *Earth, Planets and Space* **63**(7), 785–789.

Bradley, B. A. & Cubrinovski, M. (2011), 'Near-source strong ground motions observed in the 22 february 2011 christchurch earthquake', *Seismological Research Letters* **82**(6), 853–865.

Campillo, M., Gariel, J., Aki, K. & Sanchez-Sesma, F. (1989), 'Destructive strong ground motion in mexico city: Source, path, and site effects during great 1985 michoacán earthquake', *Bulletin of the Seismological Society of America* **79**(6), 1718–1735.

Chávez-García, F. J. & Bard, P.-Y. (1994), 'Site effects in mexico city eight years after the september 1985 michoacan earthquakes', *Soil Dynamics and Earthquake Engineering* **13**(4), 229–247.

Chiaro, G., Kiyota, T., Pokhrel, R. M., Goda, K., Katagiri, T. & Sharma, K. (2015), 'Reconnaissance report on geotechnical and structural damage caused by the 2015 gorkha earthquake, nepal', *Soils and Foundations* **55**(5), 1030–1043.

Darendeli, M. B. (2001), Development of a new family of normalized modulus reduction and material damping curves, PhD thesis, The University of Texas at Austin.

Delavaud, E. (2007), Simulation numérique de la propagation d'ondes en milieu géologique complexe: application à l'évaluation de la réponse sismique du bassin de Caracas (Venezuela), PhD thesis, Institut de Physique du Globe de Paris.

Delavaud, E., Cupillard, P., Festa, G. & Vilotte, J.-P. (2006), 3d spectral element method simulations of the seismic response in the caracas basin, *in* 'Proceedings of the Third International Symposium on the Effects of Surface Geology on Seismic Motion', Grenoble, pp. 515–522.

Dupros, F., De Martin, F., Foerster, E., Komatitsch, D. & Roman, J. (2010), 'High-performance finite-element simulations of seismic wave propagation in three-dimensional nonlinear inelastic geological media', *Parallel Computing* **36**(5), 308–325.

Electric Power Research Institute, E. (1993), Guidelines for determining design basis ground motions, Technical report, Electric Power Reasearch Institute Technological Report EPRI TR-102293.

Ermert, L., Poggi, V., Burjánek, J. & Fäh, D. (2014), 'Fundamental and higher two-dimensional resonance modes of an alpine valley', *Geophysical Journal International* **198**(2), 795–811.

Faccioli, E., Maggio, F., Paolucci, R. & Quarteroni, A. (1997), '2d and 3d elastic wave propagation by a pseudo-spectral domain decomposition method', *Journal of Seismology* **1**(3), 237–251.

Festa, G. & Vilotte, J. P. (2005), 'The newmark scheme as velocity–stress time-staggering: an efficient pml implementation for spectral element simulations of elastodynamics', *Geophysical Journal International* **161**(3), 789–812.

Gandomzadeh, A. (2011), Dynamical soil-structure interactions: Influence of soil behaviour nonlinearities, PhD thesis, Université Paris-Est.

Gélis, C. & Bonilla, L. F. (2012), '2-dp–sv numerical study of soil–source interaction in a nonlinear basin', *Geophysical Journal International* **191**(3), 1374–1390.

Gélis, C. & Bonilla, L. F. (2014), 'Influence of a sedimentary basin infilling description on the 2-dp–sv wave propagation using linear and non-linear constitutive models', *Geophysical Journal International* **198**(3), 1684–1700.

Guidotti, R., Stupazzini, M., Smerzini, C., Paolucci, R. & Ramieri, P. (2011), 'Numerical study on the role of basin geometry and kinematic seismic source in 3d ground motion simulation of the 22 february 2011 mw 6.2 christchurch earthquake', *Seismological Research Letters* **82**(6), 767–782.

Haney, M., Snieder, R., Ampuero, J.-P. & Hofmann, R. (2007), 'Spectral element modelling of fault-plane reflections arising from fluid pressure distributions', *Geophysical Journal International* **170**(2), 933–951.

Hardin, B. O. & Drnevich, V. P. (1972), 'Shear modulus and damping in soils: measurement and parameter effects', *Journal of Soil Mechanics and Foundations Div* **98**(sm6).

Iai, S., Matsunaga, Y. & Kameoka, T. (1990), 'Strain space plasticity model for cyclic mobility', *Report of the port and harbour research institute* **29**, 57–83.

Iai, S., Morita, T., Kameoka, T., Matsunaga, Y. & Abiko, K. (1995), 'Response of a dense sand deposit during 1993 kushiro-oki earthquake', *Soils and Foundations* **35**(1), 115–131.

Ishibashi, M. P. & Zhang, X. (1993), 'Unified dynamic shear moduli and damping patios of sand and clay', *Soils and Foundations* **33**(1), 182–191.

Iwan, W. D. (1967), 'On a class of models for the yielding behavior of continuous and composite systems', *Journal of Applied Mechanics* **34**(3), 612–617.

Joyner, W. B. (1975), 'A method for calculating nonlinear seismic response in two dimensions', *Bulletin of the Seismological Society of America* **65**(5), 1337–1357.

Kawase, H. & Aki, K. (1989), 'A study on the response of a soft basin for incident s, p, and rayleigh waves with special reference to the long duration observed in mexico city', *Bulletin of the Seismological Society of America* **79**(5), 1361–1382.

Komatitsch, D. & Vilotte, J. P. (1998), 'The spectral element method: An efficient tool to simulate the seismic response of 2d and 3d geological structures', *Bulletin of the seismological society of America* **88**(2), 368–392.

Kristeková, M., Kristek, J., Moczo, P. & Day, S. M. (2006), 'Misfit criteria for quantitative comparison of seismograms', *Bulletin of the seismological Society of America* **96**(5), 1836–1850.

Lacave, C. & Lemeille, F. (2006), 'Seismic hazard and alpine valley response analysis : generic valley configurations', *Third international Symposium on the effects of surface geology on seismic motion. Grenoble, France, 30 August – 1 September 2006. Paper number 1.* .

Laurendeau, A., Courboulex, F., Bonilla, L. F., Alvarado, A., Naya, V. A., Guéguen, P., Mercerat, E. D., Singaucho, J. C., Bertrand, E., Perrault, M. et al. (2017), 'Low-frequency seismic amplification in the quito basin (ecuador) revealed by accelerometric recordings of the renac network', *Bulletin of the Seismological Society of America* **107**(6), 2917–2926.

Liu, P. & Archuleta, R. J. (2006), 'Efficient modeling of q for 3d numerical simulation of wave propagation', *Bulletin of the Seismological Society of America* **96**(4A), 1352–1358.

Lyakhovsky, V. & Hamiel, Y. (2009), Nonlinear elasticity and scalar damage rheology model for fractured rocks, *in* 'Meso-Scale Shear Physics in Earthquake and Landslide Mechanics', CRC Press, pp. 123–132.

Madariaga, R., Ampuero, J. & Adda-Bedia, M. (2006), 'Seismic radiation from simple models of earthquakes', *Earthquakes: Radiated energy and the physics of faulting* pp. 223–236.

Martino, S., Lenti, L., Gélis, C., Giacomi, A. C., Santisi d'Avila, M., Bonilla, L. F., Bozzano, F. & Semblat, J. F. (2015), 'Influence of lateral heterogeneities on strong-motion shear strains: Simulations in the historical center of rome (italy)', *Bulletin of the Seismological Society of America* **105**(5), 2604–2624.

Maufroy, E., Chaljub, E., Hollender, F., Kristek, J., Moczo, P., Klin, P., Priolo, E., Iwaki, A., Iwata, T., Etienne, V. et al. (2015), 'Earthquake ground motion in the mygdonian basin, greece: the e2vp verification and validation of 3d numerical simulation up to 4 hz', *Bulletin of the Seismological Society of America* .

Meng, L. & Ampuero, J.-P. (2012), 'Slow rupture and weakly pressure-sensitive strength enables compressional branching: Dynamic rupture simulations of the 2012 off-sumatra earthquake 2', *Geophys. Res. Lett* .

O'Brien, G. S. & Bean, C. J. (2011), 'An irregular lattice method for elastic wave propagation', *Geophysical Journal International* **187**(3), 1699–1707.

Olsen, K. B. & Archuleta, R. J. (1996), 'Three-dimensional simulation of earthquakes on the los angeles fault system', *Bulletin of the Seismological Society of America* **86**(3), 575–596.

Oral, E. (2016), Modélisation de la propagation des ondes sismiques dans les milieux linéaires et non-linéaires, PhD thesis, Université Paris-Est.

Oral, E., Gélis, C., Bonilla, L. F. & Delavaud, E. (2017), 'Spectral element modelling of seismic wave propagation in visco-elastoplastic media including excess-pore pressure development', *Geophysical Journal International* **211**(3), 1494–1508.

Oral, E., Lopez-Caballero, F. & Gatti, F. (2018), 3d spectral element modeling of near source effects including kinematic rupture and finite-fault effects, *in* '16th European Conference on Earthquake Engineering, Thessaloniki, Greece.'.

Peyrusse, F., Glinsky, N., Gélis, C. & Lanteri, S. (2014), A high-order discontinuous galerkin method for viscoelastic wave propagation, *in* 'Spectral and High Order Methods for Partial Differential Equations-ICOSAHOM 2012', Springer, pp. 361–371.

Pham, V. A. (2013), Effets de la pression interstitielle sur la reponse sismique des sols : modélisation numérique 1D/ 3 composantes, PhD thesis, Université Paris-Est.

Priolo, E. & Seriani, G. (1993), 'Spectral element method with substructuring: an accurate and efficient high-order finite element approach for wave modeling', *Environmental acoustics, scattering and propagation* **2**, 509–527.

Régnier, J., Bonilla, L.-F., Bard, P.-Y., Bertrand, E., Hollender, F., Kawase, H., Sicilia, D., Arduino, P., Amorosi, A., Asimaki, D. et al. (2016), 'International benchmark on numerical simulations for 1d, nonlinear site response (prenolin): Verification phase based on canonical cases', *Bulletin of the Seismological Society of America* **106**(5), 2112–2135.

Roten, D., Fäh, D. & Bonilla, L. F. (2013), 'High-frequency ground motion amplification during the 2011 tohoku earthquake explained by soil dilatancy', *Geophysical Journal International* **193**(2), 898–904.

Roten, D., Fäh, D. & Bonilla, L. F. (2014), 'Quantification of cyclic mobility parameters in liquefiable soils from inversion of vertical array records', *Bulletin of the Seismological Society of America* **104**(6), 3115–3138.

Roten, D., Fäh, D., Cornou, C. & Giardini, D. (2006), 'Two-dimensional resonances in alpine valleys identified from ambient vibration wavefields', *Geophysical Journal International* **165**(3), 889–905.

Roten, D., Olsen, K. & Pechmann, J. (2012), '3d simulations of m 7 earthquakes on the wasatch fault, utah, part ii: Broadband (0–10 hz) ground motions and nonlinear soil behavior', *Bulletin of the Seismological Society of America* **102**(5), 2008–2030.

Sánchez-Sesma, F. J. (1985), 'Diffraction of elastic sh waves by wedges', *Bulletin of the seismological society of America* **75**(5), 1435–1446.

Semblat, J. F., Kham, M., Parara, E., Bard, P.-Y., Pitilakis, K., Makra, K. & Raptakis, D. (2005), 'Seismic wave amplification: Basin geometry vs soil layering', *Soil dynamics and earthquake engineering* **25**(7-10), 529–538.

Seriani, G. & Priolo, E. (1991), High-order spectral element method for acoustic wave modeling, *in* '1991 SEG Annual Meeting', Society of Exploration Geophysicists.

Smerzini, C., Paolucci, R. & Stupazzini, M. (2011), 'Comparison of 3d, 2d and 1d numerical approaches to predict long period earthquake ground motion in the gubbio plain, central italy', *Bulletin of Earthquake Engineering* **9**(6), 2007–2029.

Smith, S. & Snieder, R. (2010), 'Seismic modeling and analysis of a prototype heated nuclear waste storage tunnel, yucca mountain, nevada', *Geophysics* **75**(1), T1–T8.

Stacey, R. (1988), 'Improved transparent boundary formulations for the elastic-wave equation', *Bulletin of the Seismological Society of America* **78**(6), 2089–2097.

Stupazzini, M., Paolucci, R. & Igel, H. (2009), 'Near-fault earthquake ground-motion simulation in the grenoble valley by a high-performance spectral element code', *Bulletin of the Seismological Society of America* **99**(1), 286–301.

Takemiya, H. & Adam, M. (1998), '2d nonlinear seismic ground analysis by fem bem: The case of kobe in the hyogo-ken nanbu earthquake', *Structural Engineering Earthquake Engineering* **15**, 19s–28s.

Tokimatsu, K., Mizuno, H. & Kakurai, M. (1996), 'Building damage associated with geotechnical problems', *Soils and foundations* **36**(Special), 219–234.

Vucetic, M. & Dobry, R. (1991), 'Effect of soil plasticity on cyclic response', *Journal of geotechnical engineering* **117**(1), 89–107.